Citation as follows :
Rexer M, Hirt C, Claessens S, Tenzer R (2016) Layer-Based Modelling of the Earth's Gravitational Potential up to 10-km Scale in Spherical Harmonics in Spherical and Ellipsoidal Approximation, *Surveys in Geophysics*, 37(6), pp 1035-1074, DOI: 10.1007/s10712-016-9382-2, Springer Netherlands

Note: This is an Author's Original Manuscript of an article whose final and definitive form, the Version of Record, has been published in Surveys in Geophysics (2016, ©Springer Netherlands) available at: `http://dx.doi.org/10.1007/s10712-016-9382-2`

Layer-based modelling of the Earth's gravitational potential up to 10km-scale in spherical harmonics in spherical and ellipsoidal approximation

Moritz Rexer[1] · **Christian Hirt**[1] · **Sten Claessens**[2] · **Robert Tenzer**[3,4]

in: *Surveys in Geophysics*, Received: May 2016 / Accepted: August 2016

Abstract Global forward modelling of the Earth's gravitational potential, a classical problem in geophysics and geodesy, is relevant for a range of applications such as gravity interpretation, isostatic hypothesis testing or combined gravity field modeling with high and ultra-high resolution. This study presents spectral forward modelling with volumetric mass layers to degree 2190 for the first time based on two different levels of approximation. In spherical approximation, the mass layers are referred to a sphere, yielding the spherical topographic potential (STP). In ellipsoidal approximation where an ellipsoid of revolution provides the reference, the ellipsoidal topographic potential (ETP) is obtained. For both types of approximation we derive a mass-layer concept and study it with layered data from the Earth2014 topography model at 5 arc-min resolution. We show that the layer concept can be applied either with actual layer density or density contrasts w.r.t. a reference density, without discernible differences in the computed gravity functionals. To avoid aliasing and

[1] Institute of Astronomical and Physical Geodesy · Institute for Advanced Study, Technische Universität München
Arcisstrasse 21, D-80333 München
Tel.: +49-(0)89-289-23190
Fax: +49-(0)89-289-23178
E-mail: m.rexer@tum.de,c.hirt@tum.de

[2] The Institute for Geoscience Research · Western Australian Geodesy Group · Department of Spatial Sciences, Curtin University
GPO Box U1987, Perth, WA 6845
Tel.: +61-(0)8-9266-3505
Fax: +61-(0)8-9266-2703
E-mail: s.claessens@curtin.edu.au

[3] The Key Laboratory of Geospace Environment and Geodesy, Wuhan University
Wuhan, China
Tel.: +86-27-6877-8649
E-mail: rtenzer@sgg.whu.edu.cn

[4] New Technologies for the Information Society (NTIS), University of West Bohemia
Plzen, Czech Republic

truncation errors, we carefully account for increased sampling requirements due to the exponentiation of the boundary functions and consider all numerically relevant terms of the involved binominal series expansions. The main outcome of our work is a set of new spectral models of the Earth's topographic potential relying on mass layer modelling in spherical and in ellipsoidal approximation. We compare both levels of approximations geometrically, spectrally and numerically and quantify the benefits over the frequently used rock-equivalent topography (RET) method. We show that by using the ETP it is possible to avoid any displacement of masses and quantify also the benefit of mapping-free modelling. The layer-based forward modelling is corroborated by GOCE satellite gradiometry, by in-situ gravity observations from recently released Antarctic gravity anomaly grids and degree correlations with spectral models of the Earth's observed geopotential. As the main conclusion of this work, the mass layer approach allows more accurate modelling of the topographic potential because it avoids 10-20 mGal approximation errors associated with RET techniques. The spherical approximation is suited for a range of geophysical applications, while the ellipsoidal approximation is preferable for applications requiring high accuracy or high resolution.

Keywords gravity forward modelling · ellipsoidal topographic potential · harmonic combination method · spherical harmonics · spherical approximation · ellipsoidal approximation · layer concept · Earth2014

1 Introduction

1.1 Motivation and related work

Global modelling of the Earth's gravitational potential from its underlying mass-distribution in spherical harmonics is a classical problem in geophysics and geodesy (e.g. Balmino et al (1973); Rapp (1982); Rummel et al (1988); Wieczorek (2007, 2015)). The solution to this problem can be used for testing of topographic/isostatic hypothesis (Rummel et al, 1988; Göttl and Rummel, 2009; Hirt et al, 2012; Grombein et al, 2014), modelling of Bouguer gravity (Balmino et al, 2012; Wieczorek, 2015; Rexer et al, 2015), smoothing or reduction of the Earth's gravity field and its observations (as e.g. needed for Stokes' geodetic boundary value problem or improved interpolation/prediction with remove-compute-restore techniques (Grombein et al, 2014)), computation of fill-in gravity for combined gravity field models (Pavlis et al, 2007, 2012; Fecher et al, 2013), omission error modelling (Hirt et al, 2011; Rexer and Hirt, 2015a) and the evaluation of digital elevation models (Rexer et al, 2015).

For some of the listed applications, a forward model that is as close as possible to the actual gravity field is desirable. Aiming at such a 'perfect' synthetic gravitational model, an accurate mass model of the Earth is required. Mass models deliver information about the physical geometry of Earth along with density information about its interior. A perfect mass model would be able to describe the masses in terms of infinitesimal small bodies (such as rectangular prisms or tesseroids) at all 3-D positions of Earth. Together with an adequate implementation of Newton's law of gravitation, which means numerical integration over all masses (see e.g.

Kuhn and Seitz (2005); Grombein et al (2014)), this mass model would allow to accurately determine the gravitational potential of Earth. However, such a mass model in reality is not practicable as the computational requirements are very challenging, and more prohibitively, because the required density and geometric information is neither available globally nor in 3-D with adequate resolution. Today, globally-consistent physical surface information (usually provided in terms of digital elevation models) at best is given with a resolution of ~ 12 m (TanDEM-X satellite mission: Bartusch et al (2008)) and a vertical accuracy of ~ 4 m (Rexer and Hirt, 2016). At short scales (~ 10 km or less) it is mainly the masses of the crust – the upper part of the lithosphere – and hydrosphere that cause substantial anomalous gravitational signals. The anomalous potential that originates from the Earth's interior (upper mantle or below) has long-wavelength character. Satellite-borne and terrestrial observation techniques result in complete (global) high-resolution models of the topographic elevation, and to some extent also of the bathymetric depth, water bodies and ice-sheets (Hirt and Rexer, 2015), making forward modelling of short-scale (=crustal) gravity signals possible to ultra-high resolution, e.g. up to ~ 2 km scale (Balmino et al, 2012) and up to ~ 200 m scale (Hirt et al, 2013).

In contrast, available density information for the lithosphere (crust and upper mantle, down to about 30 km depth) is limited to a lateral resolution of about 110 km (CRUST1.0 (Laske et al, 2012) and LITHO1.0 (Pasyanos et al, 2014)). Considering the density profile (vertical resolution), which is derived mainly from seismic tomography, presently available models only distinguish between 8 to 10 different layers, assuming that the density is not varying vertically within each layer. This short review of mass models already suggests, that it is convenient and practicable to model Earth's masses in terms of layers since layers are a natural way to describe the structure of the physical Earth.

Forward modelling can either be conducted by Newtonian integration over Earth's masses in the space domain, e.g. by using rigorous analytical integration formulas for rectangular prisms (Nagy et al, 2000, 2002) or tesseroids (Grombein et al, 2013; Heck and Seitz, 2007), or in the spectral domain, by using relations among surface spherical harmonic coefficients of the geometric boundary surfaces. Historically (Lee and Kaula, 1967; Balmino et al, 1973; Rummel et al, 1988) and recently (Wieczorek, 2007, 2015; Forsberg and Jensen, 2015; Hirt et al, 2015) forward modelling approaches were often used in combination with "single-density" mass-models, also known as rock-equivalent-topography (RET) models. RET modelling involves a compression of all masses to a layer of constant (rock) density, resulting in approximation errors in the order of several dozens of mGal, see, e.g. Grombein et al (2016) and Kuhn and Hirt (2016). Therefore, it is very useful to have forward modelling approaches that are adapted to rigorous modelling of mass layers. These are available for spatial domain modelling in spherical (Kuhn and Seitz, 2005) and ellipsoidal (Grombein et al, 2014) approximation. In spherical approximation, the topographic masses are forward-modelled relative to a mass-sphere. Correspondingly, in ellipsoidal approximation, a mass-ellipsoid as a much closer approximation of the real Earth is used to provide the reference for the forward modelling. For spectral domain modelling a layer-based approach only was formulated in spherical approximation (Pavlis and Rapp, 1990; Tenzer et al, 2010, 2015; Root et al, 2016). The spectral approach has mainly been used to create low resolution models, e.g. in

- Pavlis and Rapp (1990): to d/o 360, distinguishing between 6 different terrain types corresponding to the explicit modelling of 4 layers – topography, ocean, ice-sheets/glaciers, lake water – as represented by the OSUJAN89 topographic data base
- Tenzer et al (2010): to d/o 90, only ice-layer based on the CRUST2.0 model and the surface heights in GTOPO30 (U.S. Geological Survey, released 1996)
- Tenzer et al (2015): to d/o 180 based on the CRUST1.0 model as contained in the 9 layers – topography, ocean, polar ice sheets, sediments (3 layers) and consolidated crust (3 layers) – of *Earth's spectral crustal model* (ESCM180: Chen and Tenzer (2014))
- Tenzer et al (2016): to d/o 360 based on 4 layers – topography, ocean, inland lakes/seas and ice-sheets– of the Earth2014 model (Hirt and Rexer, 2015)
- Root et al (2016): to d/o 1800 based on 2 layers – topography and ocean – of GTOPO30

and also for ultra high-resolution modelling (Balmino et al (2012): d/o 10800 based on four layers – topography, ocean, inland lakes/seas, ice-sheets– of the ETOPO1 model (Amante and Eakins, 2009)). Note, that in the work of Balmino et al (2012), Tenzer et al (2010) and Root et al (2016) the integration is facilitated using a binominal series. In these cited works the series expansion is evaluated only up to the third order term resulting in (unknown) truncation errors (see Sec. 2.3), while Pavlis and Rapp (1990) present a rigorous integration which is more accurate but computationally more demanding, especially for high resolutions.
Recently, Claessens and Hirt (2013) have developed a spherical harmonic technique to model the Earth's gravitational potential in ellipsoidal approximation, i.e. with respect to a reference ellipsoid. In contrast to the spherical concepts of Rummel et al (1988); Pavlis and Rapp (1990); Balmino et al (2012); Wieczorek (2015); Tenzer et al (2015) – where the topograpdhic masses are considered relative to a reference sphere – the *Harmonic Combination Method* (HCM) (Claessens and Hirt, 2013) models the topographic masses considered relative to a reference ellipsoid. Thus, the HCM provides the gravity spectrum to the same level of approximation (w.r.t. the same reference) as most spherical harmonic gravity field models based on observations available at IAG's International Center for Global Earth Models (ICGEM: `http://icgem.gfz-potsdam.de/ICGEM/`). This, as will be shown, is a major advantage especially when it comes to combining and comparing the forward models with satellite data or other terrestrial data.
We may thus define – because of the underlying ellipsoidal approximation – Claessens and Hirt (2013) to provide a solution to the *ellipsoidal topographic potential* (ETP) while the methods based on a spherical approximation of the Earth's masses provide a solution to the *spherical topographic potential* (STP).
Tenzer et al (2015) and Root et al (2016) provide the framework for layer-based modelling of the STP. For the ETP such a framework is still missing. The HCM as formulated in Claessens and Hirt (2013) is designed

for a single-density mass model but it can be reformulated to adopt layer-based mass models, as will be shown in this contribution.

1.2 This work: contributions to spectral forward modelling

In this contribution we formulate a new spherical harmonic approach to compute the ETP from arbitrary volumetric layers having laterally varying density. The approach is based on the *Harmonic Combination Method* (Claessens and Hirt, 2013) and allows the layers to be referenced to the surface of some reference ellipsoid. The new approach is then validated by modelling the Earth's gravitational potential as implied by the masses of layers of the solid crust, ocean water, lake water and ice-sheets up to spherical harmonic degree 2190 (~ 10 km).

First, we recapitulate known expressions for layer-based spherical harmonic modelling of the STP (with layers referenced to the sphere) (Sec. 2.1). In the next step we make the transition from the spherical to the ellipsoidal case and formulate new expressions for layer-based spherical harmonic modelling of the ETP (with layers referenced to the ellipsoid) (Sec. 2.2). Then a layer-concept based on the layers of the Earth2014 (Hirt and Rexer, 2015) data set (Sec. 3) and two ways of applying it within the previously introduced forward modelling approaches are defined (Sec. 3.1 and 3.2). The gravitational spectra and signals of the layer-based ETP are computed with 10 km spatial resolution (Sec. 4.1) and validated using GOCE satellite gradiometry (Sec. 4.2), other gravity field models (Sec. 4.3) and terrestrial observations (Sec. 4.4). Finally, differences between the ETP and the STP are elaborated in detail (Sec. 4.5) and conclusions are drawn (Sec. 5).

2 Spectral forward modelling of the gravitational potential based on volumetric layers of laterally varying density

Let $V(P)$ be the gravitational potential at a point P exterior to the Earth's body B. Following Newton's law of gravitation and neglecting the presence of atmospheric masses, it may be written as the integral over the Earth's mass distribution (see e.g. Heiskanen and Moritz (1967); Sanso and Sideris (2013))

$$V(P) = G \int_B \frac{\rho(Q)}{l_{PQ}} \, dB \tag{1}$$

where G is the Newtonian gravitational constant, ρ (> 0) is the density value associated with the infinitesimal volume element $dB = r_B^2 \sin\theta dr d\theta d\lambda$ at Q with $Q \in B$ and l_{PQ} being the Euclidean distance between P and the respective mass-element at Q. In order to get Eq. 1 in a spherical coordinate system (P and Q are then defined by the coordinate triplet: geocentric distance r, longitude λ, co-latitude θ) the reciprocal distance $1/l_{PQ}$ has to be replaced by its spherical harmonic expansion. Rummel et al (1988) shows that Eq.

1 can then be represented as spherical harmonic series of the form

$$V(P) = \frac{GM}{R} \sum_{n=0}^{\infty} \sum_{m=-m}^{n} \left(\frac{R}{r_p}\right)^{n+1} \left\{ \frac{1}{M(2n+1)} \int_B \left(\frac{r_Q}{R}\right)^n \rho(Q)\, \overline{Y}_{nm}(\theta_Q, \lambda_Q)\, dB \right\} \overline{Y}_{nm}(\theta_P, \lambda_P) \quad (2)$$

with the mass of Earth M, its mean radius R, the geocentric radii of the computation point r_P and the source point r_Q, the spherical harmonic degree n and order m. $\overline{Y}_{nm}$ denote the well-known set of fully-normalised Laplace's surface spherical harmonic functions

$$\overline{Y}_{nm}(\theta, \lambda) = \overline{P}_{nm}(\cos\theta) \begin{cases} cos(m\lambda) & for\ m \leq 0 \\ sin(m\lambda) & for\ m > 0 \end{cases} \quad (3)$$

with $\overline{P}_{nm}$ being the fully-normalised (4π-normalised) associated Legendre functions of the first kind. The term in curly brackets in Eq. 2 now contains the integration over the Earth's mass distribution and can alternatively be represented as a set of dimensionless fully-normalised coefficients

$$\overline{V}_{nm} = \frac{3}{\overline{\rho} R^3 (2n+1)} \frac{1}{4\pi} \int_B \left(\frac{r_Q}{R}\right)^n \rho(\theta_Q, \lambda_Q)\, \overline{Y}_{nm}(\theta_Q, \lambda_Q)\, dB, \quad (4)$$

that can be subdivided into their cosine- and sine-assigned equivalents, C_{nm} and S_{nm}, according to Eq. 3, where M is replaced by $4/3\pi\overline{\rho}R^3$ and with $\overline{\rho}$ being the mean density of Earth. Then Eq. 2 can be re-written conveniently as

$$V(P) = \frac{GM}{R} \sum_{n}^{\infty} \sum_{m=-m}^{n} \left(\frac{R}{r_p}\right)^{n+1} \overline{V}_{nm} \overline{Y}_{nm}(\theta_P, \lambda_P). \quad (5)$$

Now, let's consider an Earth that is subdivided into a set of volumetric mass layers Ω_ω ($\omega = [1, 2, ..., \omega_{max}]$) fulfilling the following requirements:

(i) ρ varying only in the lateral direction in each layer ($\rho^{(\Omega_\omega)}$ is radially invariant: $\rho^{(\Omega_\omega)}(\theta, \lambda)$),

(ii) each layer having a defined upper bound (UB) and lower bound (LB) ($r_{LB}^{(\Omega_\omega)} \leq r_{UB}^{(\Omega_\omega)}$),

(iii) the layer's boundaries being entirely inside Earth's body ($r_{UB}^{(\Omega_\omega)} \leq r_B$)

(iv) the layers being uniquely separated by their boundaries ($\Omega_\omega \cap \Omega_{\omega+1} \equiv 0$),

(v) and the set of layers (including the remaining volumetric body inside the lower most layer boundary) forms a complete subset of Earth's body ($\sum_\omega \Omega_\omega \equiv B$).

Then the gravitational potential $V(P)$ in Eq. 5 may be written as a sum of the gravitational potential of each layer $V(P)^{(\Omega_\omega)}$

$$\begin{aligned}
V(P) = \sum_\omega V(P)^{(\Omega_\omega)} = \frac{GM}{R}\sum_n^\infty \sum_{m=-m}^n \left(\frac{R}{r_p}\right)^{n+1} \overline{V}_{nm}^{(\Omega_1)}\overline{Y}_{nm}(\theta_P,\lambda_P) + \\
+\frac{GM}{R}\sum_n^\infty \sum_{m=-m}^n \left(\frac{R}{r_p}\right)^{n+1} \overline{V}_{nm}^{(\Omega_2)}\overline{Y}_{nm}(\theta_P,\lambda_P) + \\
+ \ldots + \\
+\frac{GM}{R}\sum_n^\infty \sum_{m=-m}^n \left(\frac{R}{r_p}\right)^{n+1} \overline{V}_{nm}^{(\Omega_{max})}\overline{Y}_{nm}(\theta_P,\lambda_P) = \\
= \frac{GM}{R}\sum_n^\infty \sum_{m=-m}^n \left(\frac{R}{r_p}\right)^{n+1} \sum_\omega \overline{V}_{nm}^{(\Omega_\omega)}\overline{Y}_{nm}(\theta_P,\lambda_P).
\end{aligned} \tag{6}$$

Thus, the fully-normalised coefficients in Eqs. 4 and 9 are the sum of the respective coefficients of all layers

$$\overline{V}_{nm} = \sum_\omega \overline{V}_{nm}^{(\Omega_\omega)} \tag{7}$$

The fully-normalised potential coefficients of a layer $\overline{V}_{nm}^{(\Omega_\omega)}$ are given by the global radial integration of the layer's masses

$$\begin{aligned}
\overline{V}_{nm}^{(\Omega_\omega)} = \frac{3}{\overline{\rho}R^3(2n+1)}\,\frac{1}{4\pi}\int_{\Omega_\omega}\left(\frac{r_Q}{R}\right)^n \rho^{(\Omega_\omega)}(\theta_Q,\lambda_Q)\,\overline{Y}_{nm}(\theta_Q,\lambda_Q)\,d\Omega_\omega = \\
= \frac{3}{\overline{\rho}R^3(2n+1)}\,\frac{1}{4\pi}\int_{\lambda=0}^{2\pi}\int_{\theta=0}^{\pi}\int_{r_{LB}^{(\Omega_\omega)}}^{r_{UB}^{(\Omega_\omega)}}\left(\frac{r_Q}{R}\right)^n \rho^{(\Omega_\omega)}(\theta_Q,\lambda_Q)\,\overline{Y}_{nm}(\theta_Q,\lambda_Q)\,r_Q^2\sin\theta drd\theta d\lambda
\end{aligned} \tag{8}$$

where $\rho^{(\Omega_\omega)}$ denotes the layers density distribution. With moving the reference radius outside the integrals we then write (see Rummel et al (1988))

$$\overline{V}_{nm}^{(\Omega_\omega)} = \frac{3}{\overline{\rho}R(2n+1)}\,\frac{1}{4\pi}\int_{\lambda=0}^{2\pi}\int_{\theta=0}^{\pi}\Omega^{(\omega)}\,\overline{Y}_{nm}(\theta_Q,\lambda_Q)\,\sin\theta d\theta d\lambda \tag{9}$$

where $\Omega^{(\omega)}$ denotes the radial integration of the layer's masses

$$\Omega^{(\omega)} = \int_{r_{LB}^{(\Omega_\omega)}}^{r_{UB}^{(\Omega_\omega)}}\left(\frac{r_Q}{R}\right)^{n+2} \rho^{(\Omega_\omega)}(\theta_Q,\lambda_Q)\,dr. \tag{10}$$

Since $\rho^{(\Omega_\omega)}$ is assumed to be a function of λ and θ only (and thus constant in radial direction within each layer), the solution of the integral in Eq. 10 yields

$$\Omega^{(\omega)} = \rho^{(\Omega_\omega)}(\theta_Q,\lambda_Q)\,\frac{R}{n+3}\left[\left(\frac{r_{UB}^{(\Omega_\omega)}}{R}\right)^{n+3} - \left(\frac{r_{LB}^{(\Omega_\omega)}}{R}\right)^{n+3}\right]. \tag{11}$$

Then consider, that the integral in Eq. 10 can also be defined with respect to the ellipsoidal radius by two separate integrals, e.g. by

$$\Omega^{(\omega)} = \int_{r=r_{LB}^{(\Omega_\omega)}}^{r_e} \left(\frac{r_Q}{R}\right)^{n+2} \rho^{(\Omega_\omega)}(\theta_Q, \lambda_Q)\, dr \;+\; \int_{r=r_e}^{r_{UB}^{(\Omega_\omega)}} \left(\frac{r_Q}{R}\right)^{n+2} \rho^{(\Omega_\omega)}(\theta_Q, \lambda_Q)\, dr. \tag{12}$$

The above (split) integral solution holds for all possible vertical arrangements of layer boundaries (where all, none or only a part of the masses of a layer are located within the reference ellipsoid), as shown in Claessens and Hirt (2013) for single-layer modelling. Then, with $\rho^{(\Omega_\omega)}$ being radially invariant, the solution to the integral in Eq. 12 becomes

$$\Omega^{(\omega)} = \rho^{(\Omega_\omega)}(\theta_Q, \lambda_Q)\, \frac{R}{n+3} \left(\left[\left(\frac{r_{UB}^{(\Omega_\omega)}}{R}\right)^{n+3} - \left(\frac{r_e}{R}\right)^{n+3} \right] - \left[\left(\frac{r_{LB}^{(\Omega_\omega)}}{R}\right)^{n+3} - \left(\frac{r_e}{R}\right)^{n+3} \right] \right), \tag{13}$$

which essentially is the same as Eq. 11, since $\left(\frac{r_e}{R}\right)^{n+3}$ cancels out in Eq. 13. Starting from this solution to the radial integral of the masses within a layer Ω_ω – which will turn out to be of mathematically convenient form – we will derive the potential $V(P)^{(\Omega_\omega)}$ of a volumetric layer in spherical approximation in section 2.1 and in ellipsoidal approximation in section 2.2.

2.1 Layer-based modelling with respect to a reference sphere

The potential based on volumetric layers of laterally variable density as given by Eq. 6 modelled with respect to a reference sphere means – in simple words – a spherical approximation of Earth's masses and yields the *spherical topographic potential* V^{STP}. A solution to the layer-based STP was given already by Pavlis and Rapp (1990), Tenzer et al (2015) and other works (see Sect. 1) and is recapitulated in own notation here. The first spherical approximation that is introduced is setting

$$r_e = R \tag{14}$$

in Eq. 13, which yields the spherical approximated mass of the layer

$$\Omega^{(STP,\omega)} = \rho^{(\Omega_\omega)}(\theta_Q, \lambda_Q) \frac{R}{n+3} \left(\left[\left(\frac{r_{UB}^{(\Omega_\omega)}}{R}\right)^{n+3} - 1 \right] - \left[\left(\frac{r_{LB}^{(\Omega_\omega)}}{R}\right)^{n+3} - 1 \right] \right). \tag{15}$$

The second spherical approximation is made by describing the layer's boundaries with respect to the reference sphere as

$$\begin{aligned} r_{UB}^{(\Omega_\omega)} &= R + H_{UB}^{(\Omega_\omega)} \\ r_{LB}^{(\Omega_\omega)} &= R + H_{LB}^{(\Omega_\omega)} \end{aligned} \tag{16}$$

where $H_{UB}^{(\Omega_\omega)}$ and $H_{LB}^{(\Omega_\omega)}$ denote the orthometric height of the upper and the lower boundary of Ω_ω, respectively. We may then introduce the well known binominal expansion for both terms in square brackets in Eq. 15 (see Rummel et al (1988))

$$\begin{aligned}
\left(\frac{r_{UB}^{(\Omega_\omega)}}{R}\right)^{n+3} - 1 &= \sum_{k=1}^{n+3} \begin{pmatrix} n+3 \\ k \end{pmatrix} \left(\frac{H_{UB}^{(\Omega_\omega)}}{R}\right)^k = \sum_{k=1}^{n+3} \frac{1}{k!} \prod_{i=1}^{k} (n+4-i) \left(\frac{H_{UB}^{(\Omega_\omega)}}{R}\right)^k \\
\left(\frac{r_{LB}^{(\Omega_\omega)}}{R}\right)^{n+3} - 1 &= \sum_{k=1}^{n+3} \begin{pmatrix} n+3 \\ k \end{pmatrix} \left(\frac{H_{LB}^{(\Omega_\omega)}}{R}\right)^k = \sum_{k=1}^{n+3} \frac{1}{k!} \prod_{i=1}^{k} (n+4-i) \left(\frac{H_{LB}^{(\Omega_\omega)}}{R}\right)^k
\end{aligned} \tag{17}$$

and yield

$$\begin{aligned}
\Omega^{(STP,\omega)} &= \rho^{(\Omega_\omega)}(\theta_Q,\lambda_Q)\frac{R}{n+3}\left(\sum_{k=1}^{n+3}\begin{pmatrix} n+3 \\ k \end{pmatrix}\left(\frac{H_{UB}^{(\Omega_\omega)}}{R}\right)^k - \sum_{k=1}^{n+3}\begin{pmatrix} n+3 \\ k \end{pmatrix}\left(\frac{H_{LB}^{(\Omega_\omega)}}{R}\right)^k\right) = \\
&= \rho^{(\Omega_\omega)}(\theta_Q,\lambda_Q)\frac{R}{n+3}\sum_{k=1}^{n+3}\begin{pmatrix} n+3 \\ k \end{pmatrix}\left(\left(\frac{H_{UB}^{(\Omega_\omega)}}{R}\right)^k - \left(\frac{H_{LB}^{(\Omega_\omega)}}{R}\right)^k\right).
\end{aligned} \tag{18}$$

Inserting Eq. 18 into Eq. 9 gives, after moving the double integral into the binominal series, the solution to the layer's spherical topographic potential

$$\begin{aligned}
\overline{V}_{nm}^{(STP,\Omega_\omega)} &= \frac{3}{\overline{\rho}(2n+1)(n+3)}\sum_{k=1}^{n+3}\begin{pmatrix} n+3 \\ k \end{pmatrix} \times \\
&\times \frac{1}{4\pi}\int_{\lambda=0}^{2\pi}\int_{\theta=0}^{\pi}\rho^{(\Omega_\omega)}(\theta_Q,\lambda_Q)\left(\left(\frac{H_{UB}^{(\Omega_\omega)}}{R}\right)^k - \left(\frac{H_{LB}^{(\Omega_\omega)}}{R}\right)^k\right)\overline{Y}_{nm}(\theta_Q,\lambda_Q)\sin\theta d\theta d\lambda
\end{aligned} \tag{19}$$

where the height function (HF) to the power k within the double integral, scaled by the density $\rho^{(\Omega_\omega)}(\theta_Q,\lambda_Q)$ in each cell, can be expressed as a series of (fully-normalised) surface spherical harmonic coefficients of the layer's height-density function (HDF)

$$\overline{HDF}_{knm}^{(STP,\Omega\omega)} = \frac{1}{4\pi}\int_{\lambda=0}^{2\pi}\int_{\theta=0}^{\pi}\rho^{(\Omega_\omega)}(\theta_Q,\lambda_Q)\left(\left(\frac{H_{UB}^{(\Omega_\omega)}}{R}\right)^k - \left(\frac{H_{LB}^{(\Omega_\omega)}}{R}\right)^k\right)\overline{Y}_{nm}(\theta_Q,\lambda_Q)\sin\theta d\theta d\lambda. \tag{20}$$

Then we arrive at a concise expression of the layer's spherical topographic potential

$$\overline{V}_{nm}^{(STP,\Omega_\omega)} = \frac{3}{\overline{\rho}(2n+1)(n+3)}\sum_{k=1}^{n+3}\begin{pmatrix} n+3 \\ k \end{pmatrix}\overline{HDF}_{knm}^{(STP,\Omega\omega)}. \tag{21}$$

Note that the radial integration (Eq. 10) can also be done rigorously (without using binominal series expansions), as shown e.g. by Pavlis and Rapp (1990). However, the rigorous integration is much less efficient compared to an integration based on binominal series expansions (Rummel et al, 1988). Therefore, especially for large n_{max}, the rigorous approach may become excessively computationally demanding. The rigorous expressions in our notation are found in appendix A.

2.2 Layer-based modelling with respect to a reference ellipsoid

Next, the potential based on volumetric layers of laterally variable density as given by Eq. 6 is modelled with respect to a reference ellipsoid. This procedure yields the *ellipsoidal topographic potential* V^{ETP}. In contrast to the spherical variant described in Section 2.1 this modelling technique defines the layered masses with respect to a reference ellipsoid. The Earth is thus not approximated by a sphere and the true physical shape of Earth can be preserved.

The solution to the layer-based ETP discussed next is based on the HC-method derived in Claessens and Hirt (2013), who applied the HC-method only to compute the ETP from a single-density (RET) model.

The starting point is Eq. 13 that is a solution to the radial integral of a layer's masses (Eq. 10) with respect to an ellipsoid, which can also be written as follows:

$$\Omega^{(ETP,\omega)} = \rho^{(\Omega_\omega)}(\theta_Q,\lambda_Q)\frac{R}{n+3}\left(\frac{r_e}{R}\right)^{n+3}\left(\left[\left(\frac{r_{UB}^{(\Omega_\omega)}}{r_e}\right)^{n+3} - 1\right] - \left[\left(\frac{r_{LB}^{(\Omega_\omega)}}{r_e}\right)^{n+3} - 1\right]\right). \quad (22)$$

The layer's boundaries in the ellipsoidal case may be described by their pseudo-ellipsoidal heights $h'^{(\Omega_\omega)}_{UB}$ and $h'^{(\Omega_\omega)}_{LB}$ following

$$\begin{aligned} r_{UB}^{(\Omega_\omega)} &= r'_e + h'^{(\Omega_\omega)}_{UB} \\ r_{LB}^{(\Omega_\omega)} &= r'_e + h'^{(\Omega_\omega)}_{LB} \end{aligned} \quad (23)$$

measured along the direction towards the origin of the ellipsoid, akin to the geocentric coordinates needed for spherical harmonics (denoted approximate ellipsoidal height in Claessens and Hirt (2013)). In approximation the layer's boundaries may be described by $d_{UB}^{(\Omega_\omega)}$ and $d_{LB}^{(\Omega_\omega)}$ denoting the ellipsoidal height h taken in the direction towards the geocenter and thus yields

$$\begin{aligned} r_{UB}^{(\Omega_\omega)} &= r_e + d_{UB}^{(\Omega_\omega)} \\ r_{LB}^{(\Omega_\omega)} &= r_e + d_{LB}^{(\Omega_\omega)}. \end{aligned} \quad (24)$$

The error of this ellipsoidal approximation, when $d_{UB}^{(\Omega_\omega)}$ and $d_{LB}^{(\Omega_\omega)}$ are used instead $h'^{(\Omega_\omega)}_{UB}$ and $h'^{(\Omega_\omega)}_{LB}$, is investigated in Sec. 4.5.

Both square brackets terms in Eq. 22 can – equivalent to the spherical case (Eq. 17) – be expressed by the binominal series expansions

$$\begin{aligned}
\left(\frac{r_{UB}^{(\Omega_\omega)}}{r_e}\right)^{n+3} - 1 &= \sum_{k=1}^{n+3} \begin{pmatrix} n+3 \\ k \end{pmatrix} \left(\frac{d_{UB}^{(\Omega_\omega)}}{r_e}\right)^{k} = \sum_{k=1}^{n+3} \frac{1}{k!} \prod_{i=1}^{k} (n+4-i) \left(\frac{d_{UB}^{(\Omega_\omega)}}{r_e}\right)^{k} \\
\left(\frac{r_{LB}^{(\Omega_\omega)}}{r_e}\right)^{n+3} - 1 &= \sum_{k=1}^{n+3} \begin{pmatrix} n+3 \\ k \end{pmatrix} \left(\frac{d_{LB}^{(\Omega_\omega)}}{r_e}\right)^{k} = \sum_{k=1}^{n+3} \frac{1}{k!} \prod_{i=1}^{k} (n+4-i) \left(\frac{d_{LB}^{(\Omega_\omega)}}{r_e}\right)^{k} .
\end{aligned} \tag{25}$$

Inserting Eq. 25 and Eq. 22 into Eq. 9 gives a preliminary solution to the ETP of a layer

$$\begin{aligned}
\overline{V}_{nm}^{(ETP,\Omega_\omega)} &= \frac{3}{\overline{\rho}(2n+1)(n+3)} \sum_{k=1}^{n+3} \begin{pmatrix} n+3 \\ k \end{pmatrix} \times \\
\times \frac{1}{4\pi} \int_{\lambda=0}^{2\pi} \int_{\theta=0}^{\pi} \left(\frac{r_e}{R}\right)^{n+3} & \rho^{(\Omega_\omega)}(\theta_Q,\lambda_Q) \left(\left(\frac{d_{UB}^{(\Omega_\omega)}}{r_e}\right)^{k} - \left(\frac{d_{LB}^{(\Omega_\omega)}}{r_e}\right)^{k} \right) \overline{Y}_{nm}(\theta_Q,\lambda_Q) \sin\theta d\theta d\lambda .
\end{aligned} \tag{26}$$

In order to get a practicable solution for the ETP that is independent of any term with degree n in the exponent Claessens and Hirt (2013) have introduced a second (infinite) binominal series for $\left(\frac{r_e}{R}\right)^{n+3}$ that has been derived in Claessens (2006):

$$\left(\frac{r_e}{R}\right)^{n+3} = \left(\frac{b}{R}\right)^{n+3} \left(1 - e^2 \ \sin^2\theta\right)^{\left(-\frac{n+3}{2}\right)} = \left(\frac{b}{R}\right)^{n+3} \sum_{j=0}^{\infty} (-1)^j \begin{pmatrix} -\frac{n+3}{2} \\ j \end{pmatrix} e^{2j} \sin^{2j}\theta \tag{27}$$

where b is the semi-minor axis of the ellipsoid and e^2 is the squared first numerical eccentricity. With the help of fully-normalised *sinusoidal Legendre weight functions* $\overline{K}_{nm}^{2i,2j}$ (see e.g. Appendix A in Claessens and Hirt (2013) for more details on the recursion relations) it is evident, that

$$\sin^{2j}\theta \ \overline{Y}_{nm} = \sum_{i=-j}^{j} \overline{K}_{nm}^{2i,2j} \ \overline{Y}_{n+2i,m} . \tag{28}$$

Inserting Eq. 28 and Eq. 27 in Eq. 26 yields coefficients of the ellipsoidal topographic potential $V_{nm}^{(ETP,\Omega_\omega)}$ of the layer Ω_ω:

$$\begin{aligned}
\overline{V}_{nm}^{(ETP,\Omega_\omega)} &= \frac{3}{\overline{\rho}(2n+1)(n+3)} \left(\frac{b}{R}\right)^{n+3} \sum_{k=1}^{n+3} \begin{pmatrix} n+3 \\ k \end{pmatrix} \sum_{j=0}^{\infty} (-1)^j \begin{pmatrix} -\frac{n+3}{2} \\ j \end{pmatrix} e^{2j} \sum_{i=-j}^{j} \overline{K}_{nm}^{2i,2j} \times \\
&\times \frac{1}{4\pi} \int_{\lambda=0}^{2\pi} \int_{\theta=0}^{\pi} \rho^{(\Omega_\omega)}(\theta_Q,\lambda_Q) \left(\left(\frac{d_{UB}^{(\Omega_\omega)}}{r_e}\right)^{k} - \left(\frac{d_{LB}^{(\Omega_\omega)}}{r_e}\right)^{k} \right) \overline{Y}_{n+2i,m}(\theta_Q,\lambda_Q) \sin\theta d\theta d\lambda
\end{aligned} \tag{29}$$

Again, the term within the double integral, scaled by the density $\rho(\theta_Q,\lambda_Q)$ in each cell, can be expressed as a series of (fully-normalised) surface spherical harmonic coefficients of the layer's (ellipsoidal) height-density

	distance to reference surface (H or d)		
n	$\pm$ 9km	$\pm$ 4.5km	$\pm$ 1km
10	2	2	2
360	4	4	3
2160	10	7	4
2190	10	7	4
5400	17	11	5
10800	29	17	7

Table 1 Order of truncation k_{max} of the first binominal series (Eq. 25) at various resolutions (harmonic degree n) and locations of the layer boundary required to reduce the relative error below the 1%-level, where $a = 6378137$ m $\geq r_e \geq b = 6356752$ m.

n	$\Theta = 0°$	$\Theta = 10°$	$\Theta = 30°$	$\Theta = 45°$	$\Theta = 60°$	$\Theta = 80°$	$\Theta = 90°$
10	1	2	3	3	3	3	3
360	1	3	4	5	6	7	7
2160	1	4	8	12	15	18	18
2190	1	4	8	12	15	18	18
5400	1	5	13	21	27	33	34
10800	1	7	21	34	46	56	57

Table 2 Order of truncation j_{max} of the second binominal series (Eq. 27) at various resolutions (harmonic degree n) and co-latitude θ required to reduce the relative error below the 1%-level, where $b = 6356752$ m and $R = 6378137$ m.

function

$$\overline{HDF}^{(ETP,\Omega\omega)}_{klm} = \frac{1}{4\pi}\int_{\lambda=0}^{2\pi}\int_{\theta=0}^{\pi}\rho^{(\Omega_\omega)}(\theta_Q,\lambda_Q)\left(\left(\frac{d_{UB}^{(\Omega_\omega)}}{r_e}\right)^k - \left(\frac{d_{LB}^{(\Omega_\omega)}}{r_e}\right)^k\right)\overline{Y}_{lm}(\theta_Q,\lambda_Q)\sin\theta d\theta d\lambda \tag{30}$$

where $l = n + 2i$ and we arrive at a compact expression of the layer's ellipsoidally approximated potential

$$\overline{V}^{(ETP,\Omega_\omega)}_{nm} = \frac{3}{\overline{\rho}(2n+1)(n+3)}\left(\frac{b}{R}\right)^{n+3}\sum_{k=1}^{k_{max}}\binom{n+3}{k}\sum_{j=0}^{j_{max}}(-1)^j\binom{-\frac{n+3}{2}}{j}e^{2j}\sum_{i=-j}^{j}\overline{K}^{2i,2j}_{nm}\overline{HDF}^{(ETP,\Omega\omega)}_{klm} \tag{31}$$

where $k_{max} \leq n+3$ and $j_{max} < \infty$ denote the maximum orders of the binominal series expansions. While k_{max} and j_{max} are much smaller than the maximum harmonic degree of the model n_{max}, generally, the number of binominal terms that are required to avoid truncation errors for different modelling parameters (e.g. spatial resolution) are discussed next. The rigorous expressions for the ETP of mass layers (devoid of binominal series expansions) are given in Appendix A.

2.3 Convergence of binominal series expansions

As shown above Eq. 31 contains two binominal series expansions, one incrementing by k and one by j. The convergence of the first series (Eq. 25), which is also found in the solution of the STP for $r_e = R$ (Eq. 17), has been thoroughly studied e.g. by Sun and Sjöberg (2001) for various resolutions. Commonly, $k_{max} = 7$ is considered sufficient for degree 2160. We have studied the relative amplitudes in Eq. 17 since the series additionally depends on r_e in case of the ETP. However, for $a = 6378137$ m and $b = 6356752$ m (where

$a \geq r_e \geq b$) an identical number of terms were found to be required for different r_e. Our investigations show $k_{max} = 10$ is needed to achieve convergence at the 1% level (i.e. less than 1% truncation error) at degree 2160 (Table 1). Note, that Root et al (2016) showed that the convergence may be problematic for deep layers (e.g. upper mantle layers), with the boundaries' lower bound $<< R$. According to Root et al (2016) the problem can be overcome by reducing the reference radius R during the forward modelling of the affected layer and a subsequent rescaling of the computed coefficients.

The second series (Eq. 27), a function of degree n and the co-latitude Θ, occurs in the ETP only. Despite its infinite summations it was shown to always converge (Claessens, 2006). Looking at the amplitudes of the series's terms in a relative manner, at least $j_{max} = 18$ should be used to achieve convergence at the 1% level for degree 2160 and $\theta \in \left[0; \frac{\pi}{2}\right]$ (Table 2).

2.4 Sampling requirements of height-density functions

Special attention is required for the harmonic analysis of the layer's height-density functions (e.g. by means of quadrature (Rexer and Hirt, 2015b)) that is needed to derive the surface spherical harmonic coefficients $\overline{HDF}_{knm}^{(STP,\Omega\omega)}$ or $\overline{HDF}_{klm}^{(ETP,\Omega\omega)}$. Due to the exponentiation of the height function by k, the band-width (expressed by the maximum degree N of the original height function) increases proportionally with k, following (Hirt and Kuhn, 2014)

$$N(k) = kN. \tag{32}$$

Importantly, Eq. 32 implies that the gridded height functions need to be sampled according to k_{max} (see Sec. 2.3) in order to avoid any aliasing effects. Computing the STP to degree 2160 with $k_{max} = 7$ in an experiment (not shown here), with the grid sampling limiting the maximum degree to degree 2700, yields aliasing errors of up to ~ 20 mGal and a global root-mean-square (RMS) of 0.17 mGal. In all computations in this contribution, the increased sampling requirements are thus fully taken into account. A more detailed study of the aliasing effect is outside the scope of this paper.

3 Layer-concept based on Earth2014

The mass-layer concept using the STP and ETP framework presented in Sec. 2 can be applied with the four (geophysical) volumetric layers

Ω_1: Ice

Ω_2: Lakes

Ω_3: Ocean

Ω_4: Crust (solid rock)

while different rock-types or sediment layers shall not be considered. It is of course possible to include more layers but relevant global data sets at resolutions < 111 km are not available (see section 1.1). Note, that

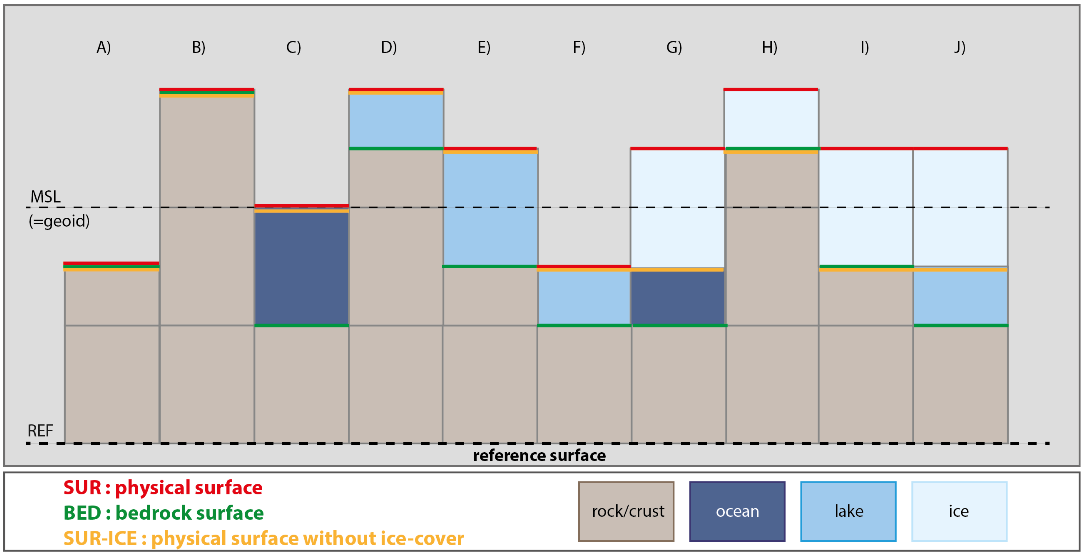

Fig. 1 Simplified scheme of the 4 geophysical layers extracted from the Earth2014 data set

vertical density functions (e.g. given by some polynomial) for the integration of ocean water columns (Tenzer et al, 2015) or radially varying mass density distributions in general (Root et al, 2016) were not integrated into the layer concept (although possible), as this is not the scope of this paper.

The layer's boundaries are generated from the Earth2014 data set (Hirt and Rexer, 2015) that provides a suite of self-consistent surface layers and masks which can be used to distinguish between ice, lake, ocean and solid Earth surface at $1'$ resolution (~ 2 km). Earth2014 is a freely-available composite model combining up-to-date digital elevation data with other gridded surface data products from different sources in terms of mean-sea-level heights. As such Earth2014 can be considered an up-to-date, higher resolution and more detailed version of the OSUJAN89 (Pavlis and Rapp, 1990), DTM2002 (Saleh and Pavlis, 2002) and ETOPO1 (Amante and Eakins, 2009) topographic data bases, that in principle provide the same terrain types (see e.g. Fig. 1 in Pavlis and Rapp (1990)). We refer to Hirt and Rexer (2015) for a full account on Earth2014 data.

In Fig. 1 a scheme of the layer-concept is given based on Earth2014 layers: *bedrock layer* (BED) describing the boundary of solid rock (green lines), *surface layer* (SUR) which is defined as the boundary between Atmosphere and Earth (red lines) and the *ice-thickness layer* (ICE). The difference between SUR and ICE describes an Earth free of ice-cover/sheets and is indicated by the orange lines. Here, a total of 10 different cases A) - J) are given showing the most common arrangement of layers w.r.t. mean sea level (MSL). Those cases and examples for occurrences on Earth are described in Table 3. Note that in both above described approaches the layer's boundaries are subject to approximation since they are defined by the orthometric height w.r.t. the respective reference surface in a spherical harmonic frame. Effectively, thus, the geoid height is neglected and the reference surface conforms with the MSL line in Fig. 1. The geometry and approximation error due to height assumptions is further discussed in section 4.5.

Two different possibilities exist for the choice of the densities, leading to the following two different approaches for layer-based forward modelling

Case	Type	Occurrence
A	dry Land – bedrock below MSL	e.g. Death Valley
B	dry Land – bedrock above MSL	most continental areas
C	ocean	all open oceans
D	lake – bedrock and lake surface above MSL	e.g. shallow parts of Great Lakes and Lake Baikal
E	lake – bedrock below MSL, lake surface above MSL	e.g. deep parts of Great Lakes and Lake Baikal
F	lake – bedrock and lake surface below MSL	e.g. Caspian Sea
G	ice shelf – ice above ocean	e.g. shorelines of Antarctica and Greenland
H	ice/snow covered bedrock above MSL	e.g. continental glaciers, Antarctica, Greenland
I	ice/snow covered bedrock below MSL	e.g. Antarctica
J	ice/snow covered lake	e.g. Lake Vostok

Table 3 Cases of layer arrangements shown in Fig. 1 and their occurrences on Earth

Layer Name	Density $[\frac{kg}{m^3}]$	Layer Boundary Type	Over Land	Over Ocean and shelf ice	Over Lakes	Over Ice
Ice-layer	917	UB	SUR	SUR	SUR	SUR
		LB	SUR-ICE	SUR-ICE	SUR-ICE	SUR-ICE
Lakes-layer	1000	UB	SUR-ICE	SUR-ICE	SUR-ICE	SUR-ICE
		LB	SUR-ICE	SUR-ICE	BED	SUR-ICE
Ocean-layer	1030	UB	SUR-ICE	SUR-ICE	SUR-ICE	SUR-ICE
		LB	SUR-ICE	BED	SUR-ICE	SUR-ICE
Crust-layer	2670	UB	BED	BED	BED	BED
		LB	REF	REF	REF	REF
Cases (c.f. Fig. 1)			A,B	C,G	D,E,F,J	H,I

Table 4 Description of layer boundaries and densities in the **LCA approach** using Earth2014 data; SUR: Earth2014 surface layer; ICE: Earth2014 Ice-thickness layer; BED: Earth2014 bedrock layer; ICE-SUR: Earth2014 surface removed for ice-sheets (see yellow lines in Fig. 1); REF: reference surface.

1) LCA: layer correction approach with actual layer densities (c.f. Table 4)

2) LRA: layer reduction approach with density contrasts (c.f. Table 5)

which are described in the following.

3.1 Layer correction approach (LCA)

In this approach, the gravitational potential generated by each mass-layer is modelled with its actual density. Each layer thus makes a (positive) contribution to the final model, i.e. the total topographic potential, that can be thought of as a *correction* in geodetic sense. Then, the total topographic potential is the sum of the potential contributions of all layers. In the LCA the layer boundaries and densities for the four layers are selected from the Earth2014 data base as listed in Table 4. The LCA can be best understood as bottom-up approach as each layer from the reference surface to the surface of Earth are modelled one after another. This is different from the approach described next.

3.2 Layer reduction approach (LRA)

One can best imagine the LRA approach as top-down approach: the crustal potential is modelled using the uppermost boundary layer (the physical surface of Earth) and is then reduced for the effect of mass-density

Layer Name	Density/ -contr. $[\frac{kg}{m^3}]$	Layer Boundary Type	Over Land	Over Ocean and shelf ice	Over Lakes	Over Ice
Crust-layer	2670	UB	SUR	SUR	SUR	SUR
		LB	REF	REF	REF	REF
Ice-layer	-1753	UB	SUR	SUR	SUR	SUR
		LB	SUR-ICE	SUR-ICE	SUR-ICE	SUR-ICE
Lakes-layer	-1670	UB	SUR-ICE	SUR-ICE	SUR-ICE	SUR-ICE
		LB	SUR-ICE	SUR-ICE	BED	SUR-ICE
Ocean-layer	-1640	UB	SUR-ICE	SUR-ICE	SUR-ICE	SUR-ICE
		LB	SUR-ICE	BED	SUR-ICE	SUR-ICE
Cases (c.f. Fig. 1)			A,B	C,G	D,E,F,J	H,I

Table 5 Description of layer boundaries and densities in the **LRA approach** using Earth2014 data; SUR: Earth2014 surface layer; ICE: Earth2014 Ice-thickness layer; BED: Earth2014 bedrock layer; ICE-SUR: Earth2014 surface removed for ice-sheets (see yellow lines in Fig. 1); REF: reference surface.

anomalies expressed by density contrasts (w.r.t. the assumed crustal density) that exist in each layer beneath the surface, down to the reference surface. The layer boundaries and density contrasts in the LRA approach are listed in Table 5. When using negative density contrasts for the layers, the total topographic potential is the sum of the gravitational effects of each layer.

3.3 LRA versus LCA

Theoretically, both approaches should yield the same potential and neither of the approaches is preferable in terms of computational expense. However, practically small differences may remain between the approaches, mainly due to spherical harmonic representation errors as will be shown (see Sect. 4.1). In literature, often only the LRA approach based on density contrasts is considered. In Tenzer et al (2015), e.g., so called *striping corrections* to the topographic correction are computed based on density contrasts, so their procedure corresponds to the LRA approach.

The cross-validation of the results of both approaches is a valuable tool for detecting inconsistencies of the used mass models. For example, consider

a) a layer A intersecting with another layer B (Fig. 2, panel a) – then the overlapping space would be modelled twice in the LCA approach and in the LRA approach, leading to different potentials: in case of LCA the overlapping space would be corrected using both layers' densities; in case of LRA the overlapping space would be reduced for both layers' density contrasts. In general, the error ϵ associated with this kind of inconsistency depends on ρ_B if UB_B is wrong, and on ρ_A if LB_A is wrong. However, no error will occur in case of the LRA if UB_B is wrong and layer B happens to be the crustal layer ($\rho_B = \rho_{crust}$).

b) a not modelled (volumetric) empty space between two layers A and B (Fig. 2, panel b) – then this space is not accounted for in the LCA approach at all, while the space is implicitly filled and modelled with crustal density in the LRA approach. Again, no error will occur in case of the LRA if UB_B is wrong and layer B happens to be the crustal layer ($\rho_B = \rho_{crust}$).

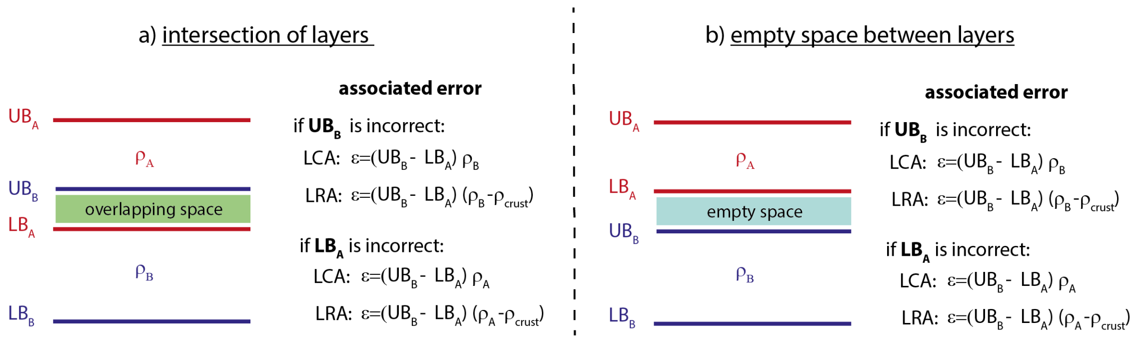

Fig. 2 Scheme and associated error of (a) intersecting layers or (b) empty space between layers in the LCA and the LRA approach.

Acronym	Approximation	Layer	Layer Approach	Max. Degree
dV_ELL_Earth2014_lca	ellipsoidal/ETP	all	LCA	2190
dV_ELL_Earth2014_lra	ellipsoidal/ETP	all	LRA	2190
dV_ELL_ICE2014_lca	ellipsoidal/ETP	Ice-layer	LCA	2190
dV_ELL_ICE2014_lra	ellipsoidal/ETP	Ice-layer	LRA	2190
dV_ELL_LAKES2014_lca	ellipsoidal/ETP	Lakes-layer	LCA	2190
dV_ELL_LAKES2014_lra	ellipsoidal/ETP	Lakes-layer	LRA	2190
dV_ELL_OCEAN2014_lca	ellipsoidal/ETP	Ocean-layer	LCA	2190
dV_ELL_OCEAN2014_lra	ellipsoidal/ETP	Ocean-layer	LRA	2190
dV_ELL_CRUST2014_lca	ellipsoidal/ETP	Crust-layer	LCA	2190
dV_ELL_CRUST2014_lra	ellipsoidal/ETP	Crust-layer	LRA	2190
dV_ELL_RET2014	ellipsoidal/ETP	all	RET	2190
dV_SPH_Earth2014_lca	spherical/STP	all	LCA	2160
dV_SPH_Earth2014_lra	spherical/STP	all	LRA	2160
dV_SPH_ICE2014_lca	spherical/STP	Ice-layer	LCA	2160
dV_SPH_ICE2014_lra	spherical/STP	Ice-layer	LRA	2160
dV_SPH_LAKES2014_lca	spherical/STP	Lakes-layer	LCA	2160
dV_SPH_LAKES2014_lra	spherical/STP	Lakes-layer	LRA	2160
dV_SPH_OCEAN2014_lca	spherical/STP	Ocean-layer	LCA	2160
dV_SPH_OCEAN2014_lra	spherical/STP	Ocean-layer	LRA	2160
dV_SPH_CRUST2014_lca	spherical/STP	Crust-layer	LCA	2160
dV_SPH_CRUST2014_lra	spherical/STP	Crust-layer	LRA	2160
dV_SPH_RET2014	spherical/STP	all	RET	2160

Table 6 Acronyms of computed potential models in the numerical study together with used layers, type of approximation, layer approach and maximum spherical harmonic degree; ETP: ellipsoidal topographic potential; STP:spherical topographic potential; LCA: layer correction approach; LRA:layer reduction approach; RET:rock-equivalent-topography (=single-density modelling)

Note that it is likewise possible (and associated with less computational costs) to detect inconsistencies in the mass models by applying the (purely) geometric conditions listed under (ii) to (v) in Sec. 2.

4 Results

This section presents a numerical study based on the ellipsoidal layer-based forward-modelling technique (Sec. 2.2) using the volumetric layers defined in Section 3. It also shows the results of the layer-based forward modelling in spherical approximation (Sec. 2.1) for comparison purposes.

Symbol	Description	LCA	LRA
$\rho^{(\Omega_1)}$	Ice-layer density/contrast	917 $\frac{kg}{m^3}$	-1753 $\frac{kg}{m^3}$
$\rho^{(\Omega_2)}$	Lakes-layer density/contrast	1000 $\frac{kg}{m^3}$	-1670 $\frac{kg}{m^3}$
$\rho^{(\Omega_3)}$	Ocean-layer density/contrast	1030 $\frac{kg}{m^3}$	-1640 $\frac{kg}{m^3}$
$\rho^{(\Omega_4)}$	Crust-layer density/contrast	2670 $\frac{kg}{m^3}$	2670 $\frac{kg}{m^3}$
$\overline{\rho}$	Earth's mean density	5495.30635355977 $\frac{kg}{m^3}$	
R	reference radius	6378137.0 m	
a	semi-major axis of GRS80	6378137.0 m	
e^2	square of first eccentricity of GRS80	0.00669438002290	
M	Earth's mass	5.972581 x 10^{24} kg	
GM	Mass x Gravitational constant	3.986005 x 10^{14} $\frac{m^3}{s^{-2}}$	
k_{max}	maximum power	12	
j_{max}	maximum summation index	30	
n_{max}	maximum degree	STP:2160; ETP:2190	
$n_{max,DEM}$	maximum degree of input Earth2014 DEM	2160	
	resolution/sampling of input Earth2014 DEM	25"	

Table 7 Constants and modelling parameters used for the numerical study

4.1 Global gravitational potential from volumetric layers in ellipsoidal approximation

The above presented techniques allow modelling the topographic gravitational potential of a single layer as well as the combined (total) effect of several layers via corrections or reductions. For the sake of clarity an overview on the computed potential fields together with their approximation level and acronyms is given in Table 6.

The dimensionless degree variances

$$c_n = \sum_{m=-n}^{n} \overline{V}_{nm}^2 \tag{33}$$

of the ETP of all layers computed using the constants given in Table 7 are shown in Fig. 3. While the single layers' potentials (colored lines) are different (by a constant scale factor) for the LRA and the LCA approach, the sum of all layer's potentials (black lines) yields similar spectra for both approaches. The difference is at least five orders of magnitude below the signal (Fig. 4, left plot), corresponding to a root-mean-square (RMS) of ~ 0.001 mGal in terms of gravity disturbances evaluated at the surface of Earth (Fig. 5). The largest differences are found above the inland lakes, which are accompanied by error patterns distributed approximately along great arcs. We believe those differences stem from spherical harmonic representation errors (Gibbs effect), that occur over small areas with large variations in height/depth (e.g. Lake Baikal). The corresponding coefficient differences are given in Fig. 4 (right plot).

We have computed a 5' global grid of gravity disturbances from the new dV_ELL_Earth2014_lca model in spectral band of degrees 0 to 2190 at the Earth's surface as represented by the Earth2014 SUR-layer. This was done by using the isGrafLab software (Bucha and Janák, 2014) along with the gradient approach for 3D harmonic synthesis (Hirt, 2012). In Fig. 6, the gravity disturbances from the dV_ELL_Earth2014_LCA model vary approximately between -802 and 624 mGal with an average signal strength (RMS) of $\sim$ 350 mGal.

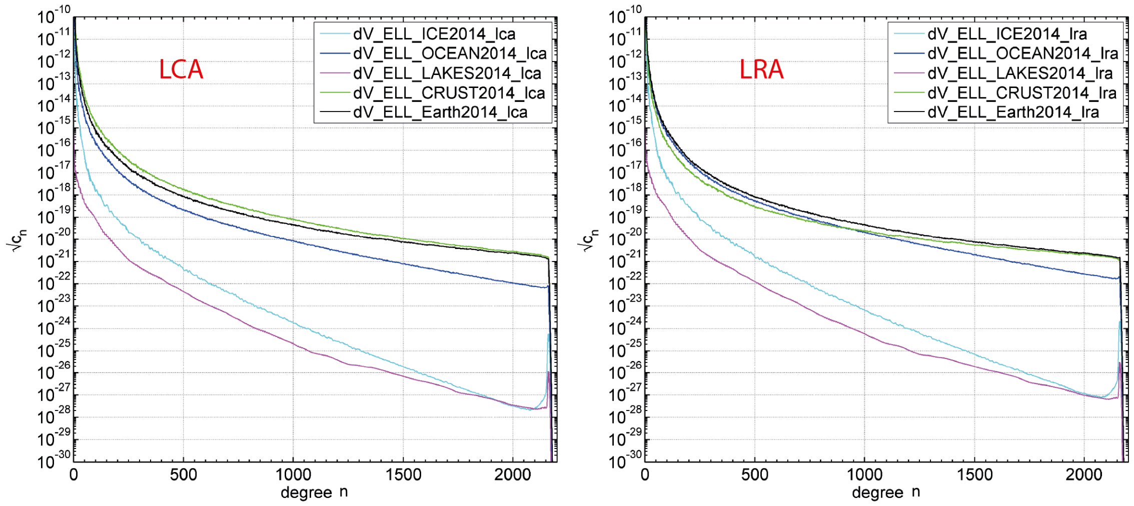

Fig. 3 Degree variances of the ellipsoidal topographic potential models and their layers using the LCA approach (left) and the LRA approach (right).

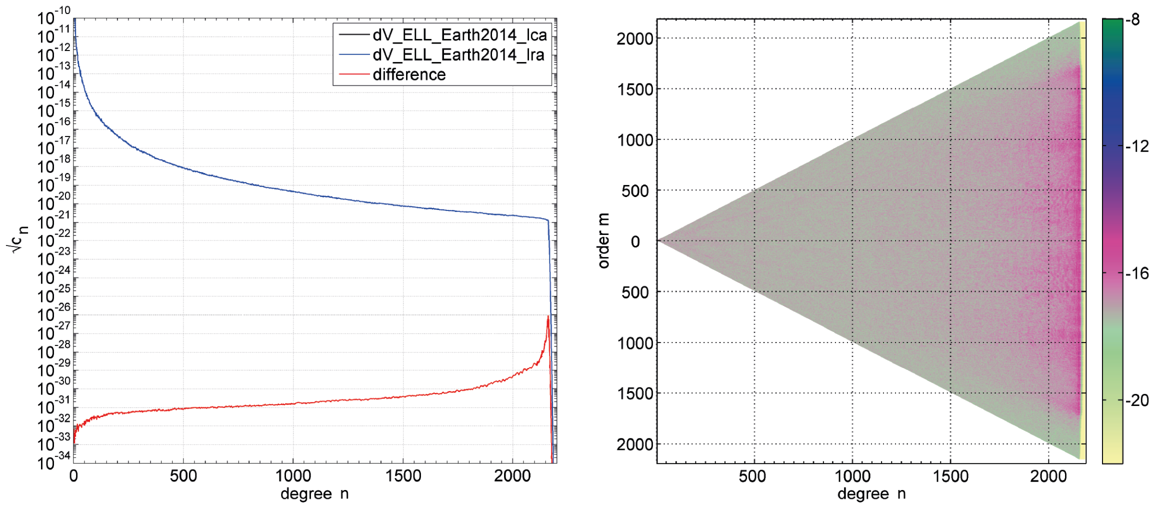

Fig. 4 LCA versus LRA approach: difference between the respective spectra of layer-based ETP in terms of degree variances (left) and dimensionless coefficient differences (right)

The area of Antarctica has been selected to show the gravitational contribution of each layer to the total gravitational effect of the Earth2014 based mass model (Fig. 7), as each layer has a significant contribution over that region. The largest contributions are given by the crust- and ocean-layer, while the ice- and lake-layer have smaller (but still) significant contributions. Note especially that e.g. the ocean layer has significant contributions over continental Antarctica (and over other continents) which underlines the importance of explicitly modelling the ocean's masses in order to retrieve a good approximation of the gravitational potential over land.

The benefit of layer-based modelling, as done here, compared to RET-based (single-density models) modelling

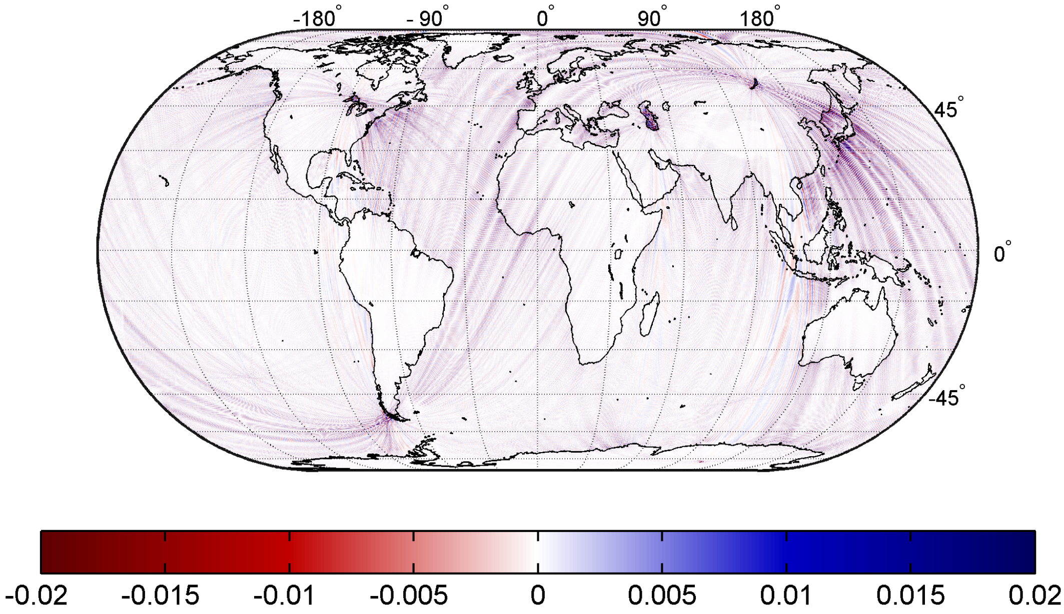

Fig. 5 LCA versus LRA approach: difference of layer-based ETP (dV_ELL_Earth2014_lca - dV_ELL_Earth2014_lra) in terms of gravity disturbances evaluated at the surface of the Earth, d/o 0..2190 (unit is in mGal). $RMS = 0.001$ mGal; $min = -0.06$ mGal; $max = 0.07$ mGal; $mean = 0.00$ mGal.

obviously is largest over ice- and water-covered parts of Earth where discrepancies are of the order of $\sim 10{-}20$ mGal (Fig. 8). Especially over the mid-oceanic ridges and deep ocean trenches (but also over many other areas) notable differences are present which all can safely be interpreted as RET approximation errors (see Sec. 4.2). The discrepancies shown in Fig. 8 are in good agreement with the findings by Grombein et al (2016) and Kuhn and Hirt (2016).

4.2 Validation of layer-based modelling using GOCE satellite gradiometry

The successful operation of a gradiometer on board of ESA satellite *Gravity Field and steady-state Ocean Circulation Explorer* (GOCE) resulted in global gravity gradient observations which currently are the most consistent and accurate source for Earth's gravity at scales up to $\sim 70{-}80$ km. Its observations as incorporated in the GOCE-only gravity field model *GO_CONS_GCF_2_TIM_R5* (EGM_TIM_R5) (Brockmann et al, 2014) are totally independent of any of the computed topographic potential models in this work and can therefore be used to quantify the benefits of layer-based modelling over RET-based modelling, thus corroborating our spectral layer approach. In this regard we compute regional *reduction rates* (RR) (Hirt et al, 2012) from $1°$

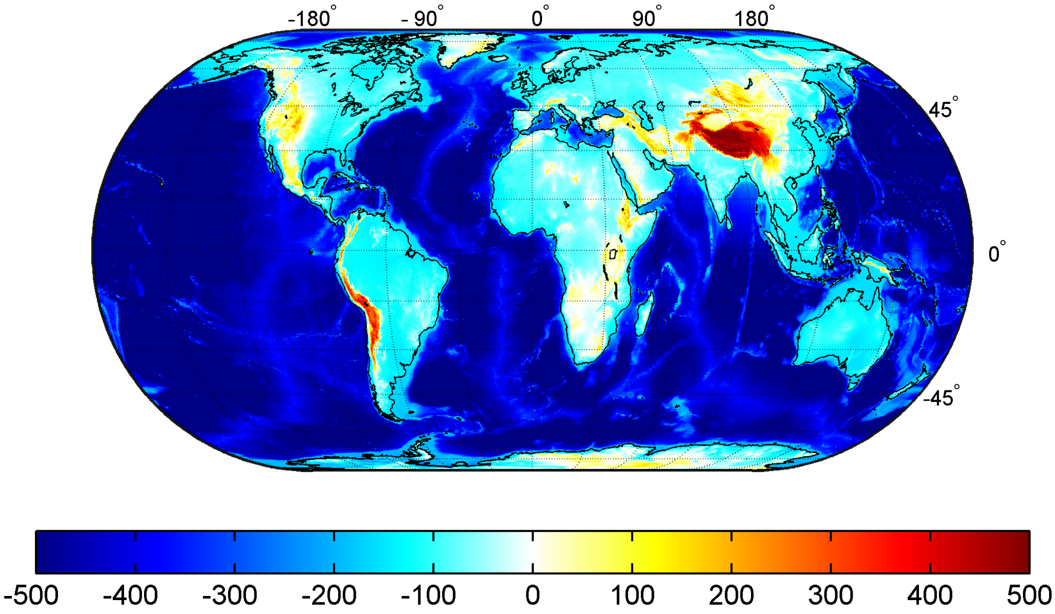

Fig. 6 Gravity of layer-based ETP (dV_ELL_Earth2014_lca) in terms of gravity disturbances evaluated at the surface of the Earth, d/o 0..2190 (unit is in mGal). $RMS = 349.45$ mGal; $min = -802.07$ mGal; $max = 623.63$ mGal; $mean = -283.58$ mGal.

x 1° blocks of band-limited gravity disturbances δg globally at the reference ellipsoid following

$$\begin{aligned} RR_{layer} &= 100 \cdot \left(1 - \frac{RMS(\delta g_{dV\_ELL\_Earth2014} - \delta g_{EGM\_TIM\_R5})}{RMS(\delta g_{EGM\_TIM\_R5})}\right) \\ RR_{RET} &= 100 \cdot \left(1 - \frac{RMS(\delta g_{dV\_ELL\_RET2014} - \delta g_{EGM\_TIM\_R5})}{RMS(\delta g_{EGM\_TIM\_R5})}\right) \end{aligned} \tag{34}$$

and investigate their differences $RR_{layer} - RR_{RET}$ (Fig. 9). The limitation of the investigation to the spectral band $n = 160...250$ is reasoned as follows: the GOCE gravity model contains the effects of isostatic compensation, that are not modelled in this work. Since isostatic effects are predominantly of long-wavelength character we exclude all degrees $n < 160$. We further exclude all degrees $n > 250$ since Brockmann et al (2014) showed that this is where the signal-to-noise ratio of the gradiometer observations becomes 1. RMS denotes the root mean square operator, applied on the respective gravity disturbances. The RR visualize to what extend the forward modelled gravity in the ETP models can be reduced (i.e. explained) by the satellite's observations. Blue areas in Fig. 9 thus are areas where the layer-modeling – in simple words – agrees better with GOCE observations than RET-based modelling. Moreover, it is interesting to see that above the continents – predominantly above near-coastal land-areas – significant improvement through the layer-based modelling was achieved, although the mass-model over the continents is the same (except of lakes) in the case of RET-based and layer-based modelling. The reason for this behavior of course is that the

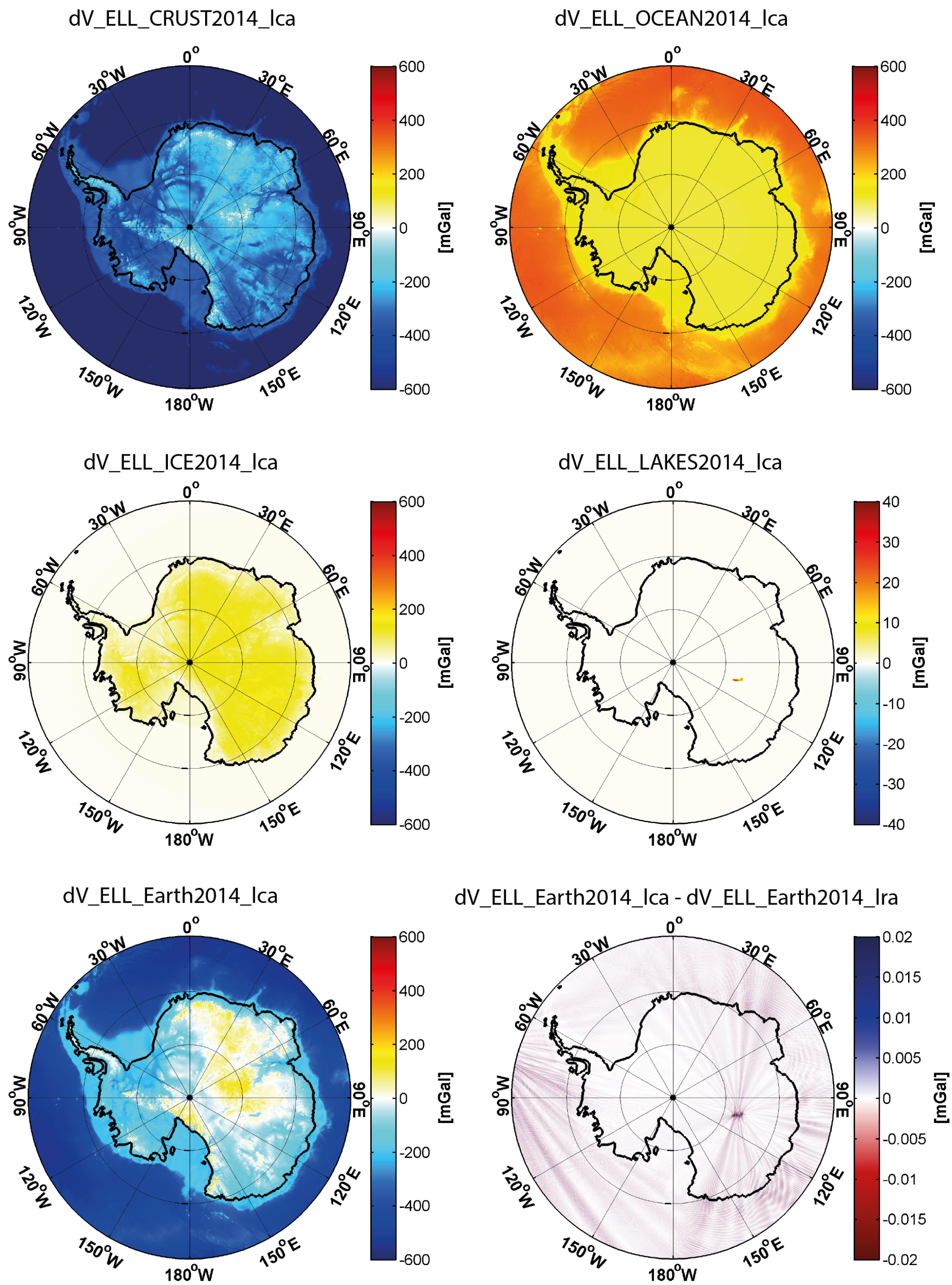

Fig. 7 Gravity contribution in terms of gravity disturbances (mGal) of the single layers, their combined effect and the difference between LCA and LRA approach over the area of Antarctica.

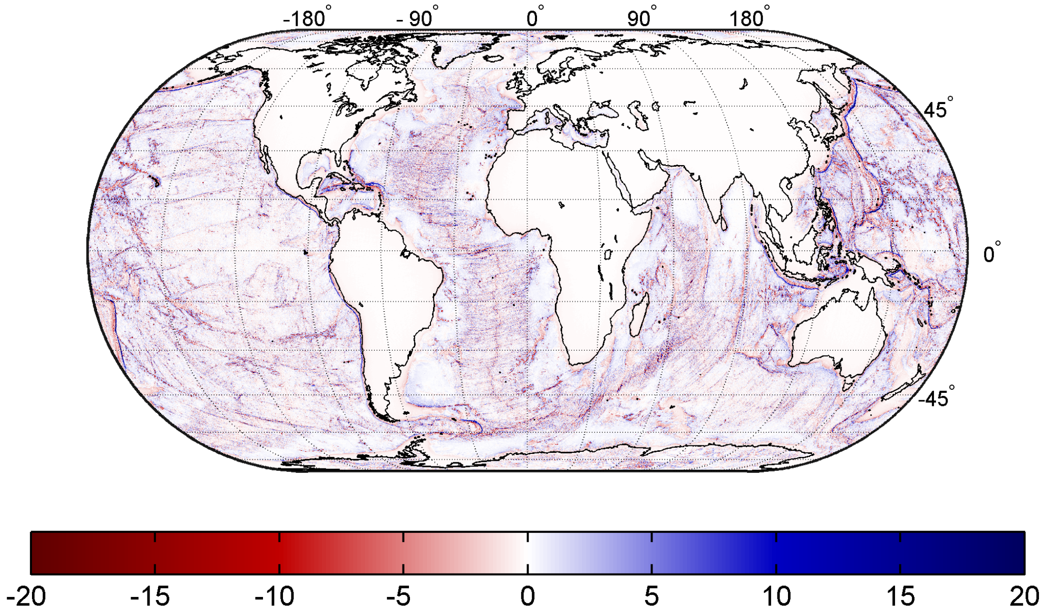

Fig. 8 Layer-based modelling versus RET-based (single-density) modelling : difference between the layer-based ETP and the RET-based ETP in terms of gravity disturbances evaluated at the reference ellipsoid (unit is in mGal). $RMS = 1.79$ mGal; $min = -45.67$ mGal; $max = 65.91$ mGal; $mean = -0.05$ mGal.

gravitational signal of a bounded density contrast (which in this case is the ocean) leaks over its physical boundaries.

4.3 Corroboration of layer-based modelling using other GGMs

Any existing global gravitational model (GGM) may be used to investigate the quality of the suggested layer-based forward modelling. We restrict our investigations to two models which are

1) EGM2008: the Earth Gravitational Model 2008 (Pavlis et al, 2012) which is a combined GGM using satellite observations, terrestrial observations and residual terrain fill-in gravity complete up to degree and order (d/o) 2190. EGM2008 incorporates the most complete (and up-to-date) set of terrestrial gravity observations of any available GGM and is therefore the best candidate to investigate the layer-based modelling at short-scales with real observations.
2) RWI_TOPO_2015: the Rock-Water-Ice topographic model 2015 (Grombein et al, 2016) is a forward-model based on layers of solid rock, water and ice derived from the same data set (Earth2014) as used for the layer-based ETP models in this work. Contrary to this work RWI_TOPO_2015 has been generated from an integration in the space domain using a tesseroid approach (see Grombein et al (2013)) and was transformed into the spectral domain by a subsequent spherical harmonic analysis. The model is

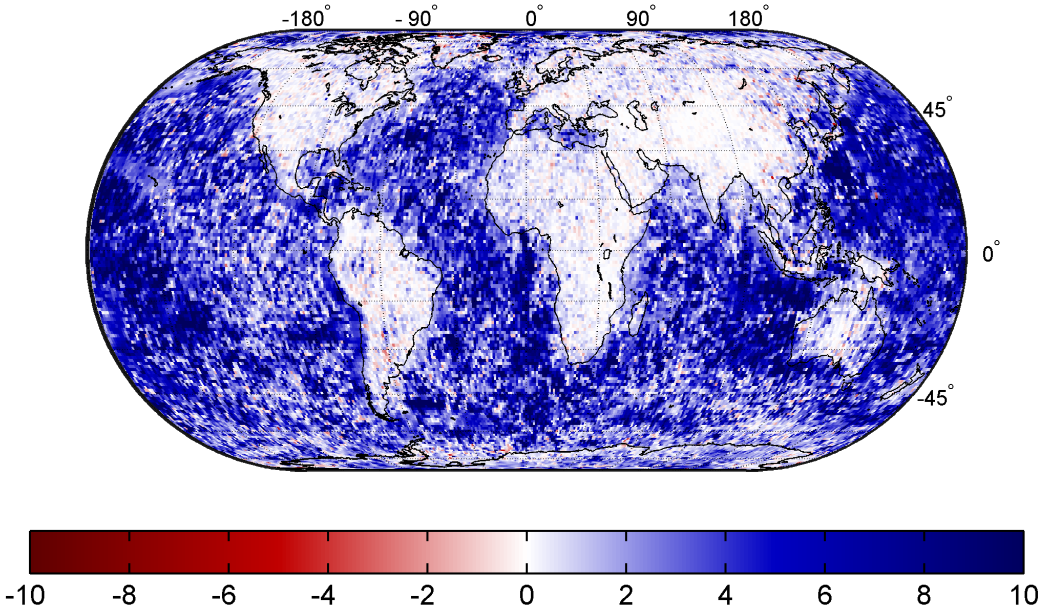

Fig. 9 Layer-based modelling versus RET-based (single-density) modelling : reduction rate differences (Eq. 34) in $1°$ x $1°$ blocks using gravity from the GOCE-only model *GO_CONS_GCF_2_TIM_R5* in the band from degree 160 to 250. Positive values denote a better agreement between layer-based modelling and GOCE observations (unit is in percent). $RMS = +5.47\%$; $average = +3.25\%$.

also complete up to d/o 2190 and is perfectly suited for a cross-validation with the suggested spectral approach in this work.

Consequently the comparison with EGM2008 will allow us to judge how closely the computed models approximate the observable gravity field at short scales while the comparison to RWI_TOPO_2015 will provide independent feedback on the modelling technique as such. The *degree correlation* (DC) y_n (see e.g. Wieczorek (2007)) of a GGM w.r.t. EGM2008 is given by

$$y_n = \frac{cx_n(EGM2008, GGM)}{\sqrt{c_n(EGM2008) \cdot c_n(GGM)}} \tag{35}$$

and indicates the degree of correlation ($[-1; 1]$) between the signal contained in coefficients of equal degree of EGM2008 and the GGM under evaluation, where cx_n is the cross degree variance

$$cx_n(EGM2008, GGM) = \sum_{m=-n}^{n} \overline{V}_{nm}(EGM2008) \cdot \overline{V}_{nm}(GGM). \tag{36}$$

As expected the computed layer-based ETP models (dV_ELL_Earth2014_lca) and RWI_TOPO_2015 show a higher correlation with EGM2008 than the RET-based model (Fig. 10 and 11). However, the degree correlation computed from the (original) spherical harmonic models reach a maximum correlation of 0.93 near degree

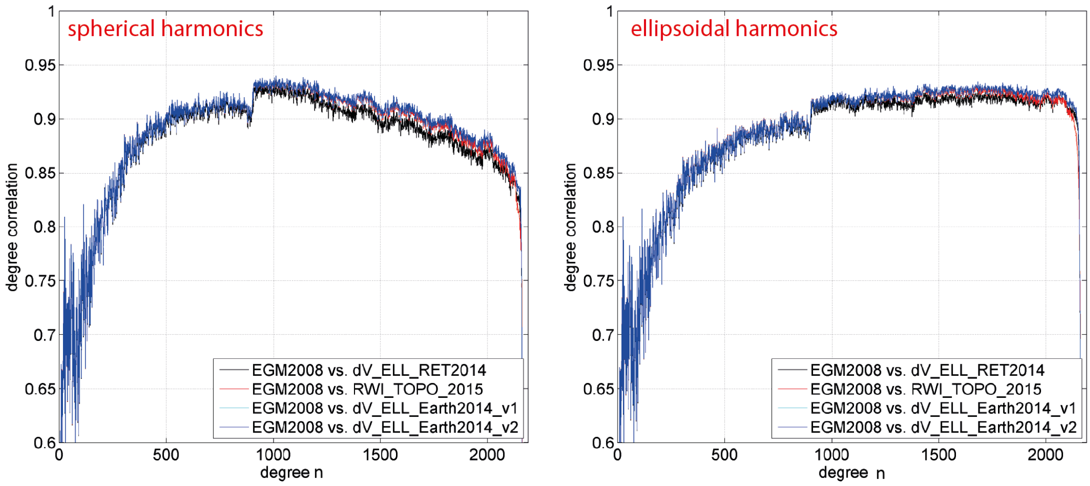

Fig. 10 Degree correlation w.r.t. EGM2008 in terms of spherical harmonic models (left panel) and in terms of their ellipsoidal harmonic equivalents (right panel).

~1000, after which the correlations decrease again (and stay above 0.8). This is against all expectations, since the short-scale signals of the gravity field are driven by the topographic masses. Hence, an increase of the correlation is to be expected. The reason for this behavior is that spherical harmonic models in ellipsoidal approximation (like EGM2008 and most other models found at ICGEM) cannot be used in small bands (band limited) because of dependencies among the coefficients that effect the ellipsoidal approximation. For instance, EGM2008 and other such models constructed in ellipsoidal approximation has to be synthesised up to degree 2190 to avoid erroneous striations increasing with latitude (also see Hirt et al (2015), Fig. 13 ibid). However, by transforming the spherical harmonic models into truly ellipsoidal harmonic models using Jekeli's transform (Jekeli, 1988), a band limited investigation of the GGMs becomes possible. Then the degree correlations stay at a high level (~ 0.92) even beyond degree ~1000 (c.f. Fig. 10, right panel), indicating that the computed layer-based ETP models agree well with the short-scale gravity as contained in EGM2008.

The difference of respective DCs reveals that the computed layer-based ETP models of this work show an increasingly higher correlation beyond degree 800 or so (up to 2% near degree 2160) compared to the RWI_TOPO_2015 model (Fig. 11). Note that a higher correlation with EGM2008 is not necessarily a valid indicator for a better quality since EGM2008 itself a) has incomplete observations over some areas (e.g. it contains only GRACE over Antarctica) and contains fill-in gravity and b) is not error-free. However, we find the degree correlations in Fig. 10 together with the findings in the previous section (4.2) to corroborate the layer-based modelling approach in this work, since the agreement with EGM2008 is at least as good as that of RWI_TOPO_2015.

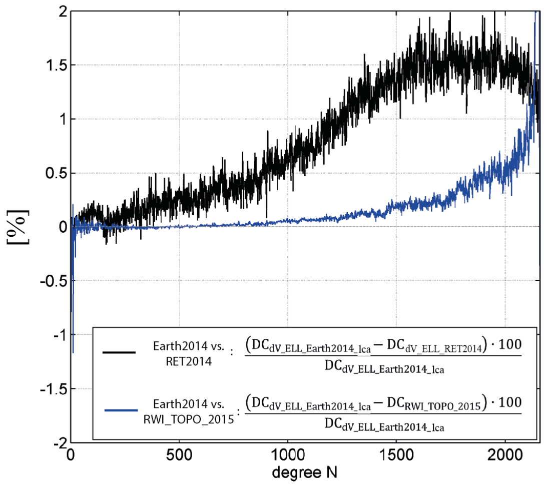

Fig. 11 Differences between the (spherical harmonic) degree correlation w.r.t. EGM2008 of RWI_TOPO_2015 (blue) and dV_ELL_RET2014 (black) versus the degree correlation of the layer-model computed in this work (dV_ELL_Earth2014_lca) in percent. Positive values denote a higher correlation of dV_ELL_Earth2014_lca.

AGAG pts (#)	Model 0..280	281..2190	Min [mGal]	Max [mGal]	Mean [mGal]	RMS [mGal]	STD [mGal]	relative to EGM2008 [%]	relative to GOCO05s [%]
total (181443)	EGM2008		-356.73	219.13	-0.02	19.61	19.61	-	-
	GOCO05s		-356.30	193.31	0.22	18.10	18.10	7.7	-
	GOCO05s	dV_ELL_RET2014	-343.15	217.33	0.28	17.90	17.90	8.7	1.1
	GOCO05s	dV_ELL_Earth2014	-342.98	217.26	0.28	17.59	17.59	10.3	2.8
	SatGravRET2014		-355.01	221.47	0.45	17.02	17.01	13.3	6.0
	SatGravEarth2014		-354.90	221.61	0.45	16.67	16.66	15.0	8.0
only continent (99410)	EGM2008		-356.73	219.13	0.02	24.56	24.56	-	-
	GOCO05s		-356.30	193.31	0.21	21.56	21.56	12.2	-
	GOCO05s	dV_ELL_RET2014	-343.16	217.33	0.14	20.63	20.63	16.0	4.3
	GOCO05s	dV_ELL_Earth2014	-342.99	217.26	0.14	20.39	20.39	17.0	5.4
	SatGravRET2014		-355.01	221.47	0.34	19.91	19.91	18.9	7.7
	SatGravEarth2014		-354.89	221.61	0.34	19.66	19.66	20.0	8.8
only ocean (82033)	EGM2008		-129.40	132.03	-0.07	10.89	10.89	-	-
	GOCO05s		-85.93	104.46	0.24	12.69	12.69	-16.5	-
	GOCO05s	dV_ELL_RET2014	-124.57	125.06	0.45	13.87	13.87	-27.4	-9.3
	GOCO05s	dV_ELL_Earth2014	-110.40	123.17	0.46	13.41	13.40	-23.0	-5.6
	SatGravRET2014		-129.81	134.08	0.59	12.65	12.63	-16.0	0.5
	SatGravEarth2014		-120.34	133.18	0.59	12.07	12.06	-10.7	5.0
AGAG STD ≤2mGal (24315)	EGM2008		-119.99	141.34	-0.01	19.10	19.10	-	-
	GOCO05s		-98.68	139.69	-0.29	17.52	17.52	8.3	-
	GOCO05s	dV_ELL_RET2014	-201.79	96.60	-0.17	15.76	15.76	17.5	10.1
	GOCO05s	dV_ELL_Earth2014	-200.29	93.12	-0.17	15.43	15.43	19.2	11.9
	SatGravRET2014		-206.96	103.41	0.17	14.65	14.65	23.3	16.4
	SatGravEarth2014		-205.40	99.22	0.18	14.30	14.30	25.1	18.4

Table 8 Descriptive statistics of residual gravity between Antarctic gravity anomaly grid (AGAG) points and various gravitational models for four different AGAG gravity data subsets.

4.4 Combination with satellite data and validation over Antarctica

For external validation with ground truth data we have computed combination models with GOCE and GRACE gravity observation data. A combination is necessary to be able to directly compare the computed layer-based forward models (see Table 6) with ground truth data, particularly at short scales. Also, because isostatic effects have rather long-wavelength character (c.f. Grombein et al (2014)) and were not taken into account in the forward modelling, satellite observations are used here as an accurate source of such information. We use precomputed normal equation matrices for GRACE (ITG-Grace2010: Mayer-Gürr et al (2010)) and GOCE (fifth release of time-wise method:Brockmann et al (2014)) along with the combination strategy described in Hirt et al (2015) (Eqs. 5-8) to create a combined model of 1) a layer-based ETP model and 2) GRACE and GOCE information that is optimal over the area of Antarctica (and to be used with care outside this area, since the ETP is likely to possess a too strong weight in some spectral bands there). The combination in principle means a regularization of (non-regularized) GOCE and GRACE normal-equations using ETP coefficients with empirically designed regularization weights. We choose the weighting scheme A in Hirt et al (2015), which was found superior especially within the polar gap region of GOCE. The combination of GRACE and GOCE with the model dV_ELL_RET2014 and dV_ELL_Earth2014_lca are named SatGravRet2014 and SatGravEarth2014, respectively. Importantly, a combination of this kind is not possible with spherically approximated (STP) models, since the levels of approximation of the satellite component and the topography component would not be consistent (see Sect. 4.5).

We compared the combined models with gravity observations as contained in the newly released Antarctic gravity anomaly grids (AGAG) (Scheinert et al, 2016). The AGAG data set is based on 13 million observations and covers an area of $1 \cdot 10^7$ km^2, corresponding to 73 % of the Antarctic continent (Fig. 12). We therefore synthesise the gravity anomaly at each AGAG point of height h above the reference surface from both combination models up to their maximum degree of resolution (d/o 2190). We also compute the gravity anomaly from the model EGM2008 (Pavlis et al, 2012) and the satellite-only model GOCO05s (Pail et al, 2011; Mayer-Gürr et al, 2015). The residuals – the differences between the AGAG data and the synthesised gravity – are taken here as an indicator of how close the observed potential (via AGAG) is represented by the different modelling variants. In case of the combination models, the differences between the AGAG gravity and modelled gravity can also be interpreted as short-scale Bouguer gravity: the AGAG observations are (more or less) completely reduced by the observed satellite gravity in the long wavelengths; in the short wavelengths the AGAG gravity is reduced for the gravitational effect of the visible topographic masses (=Bouguer gravity).

For the entire AGAG data set (181443 grid points) and a subset of the most accurate grid points (24315 grid points with standard deviation ($STD < 2$ mGal) the residuals reveal that the herein created combination model based on the layer-approach (SatGravEarth2014) performs better than the other models under investigation (Tab. 8). The improvement of SatGravEarth2014 w.r.t. EGM2008 is 15 % using all AGAG points and 25 % using the more accurate subset of points, while it improves over GOCO05s with 8 % using all points and 18.5% in the subset. The improvement of layer-based modelling w.r.t. RET modelling is about 2 % over both areas in Antarctica, which corresponds to an RMS/STD of ~ 0.3 mGal. The improvement is not very large in absolute terms but still indicative, given the differences between SatGravRet2014 and SatGravEarth2014 gravity at the AGAG points (Fig. 12) have an RMS of ~ 1 mGal only. Further, the positive effect of layer-based modelling is more notable over the ocean (5% improvement) than over land/continental Antarctica

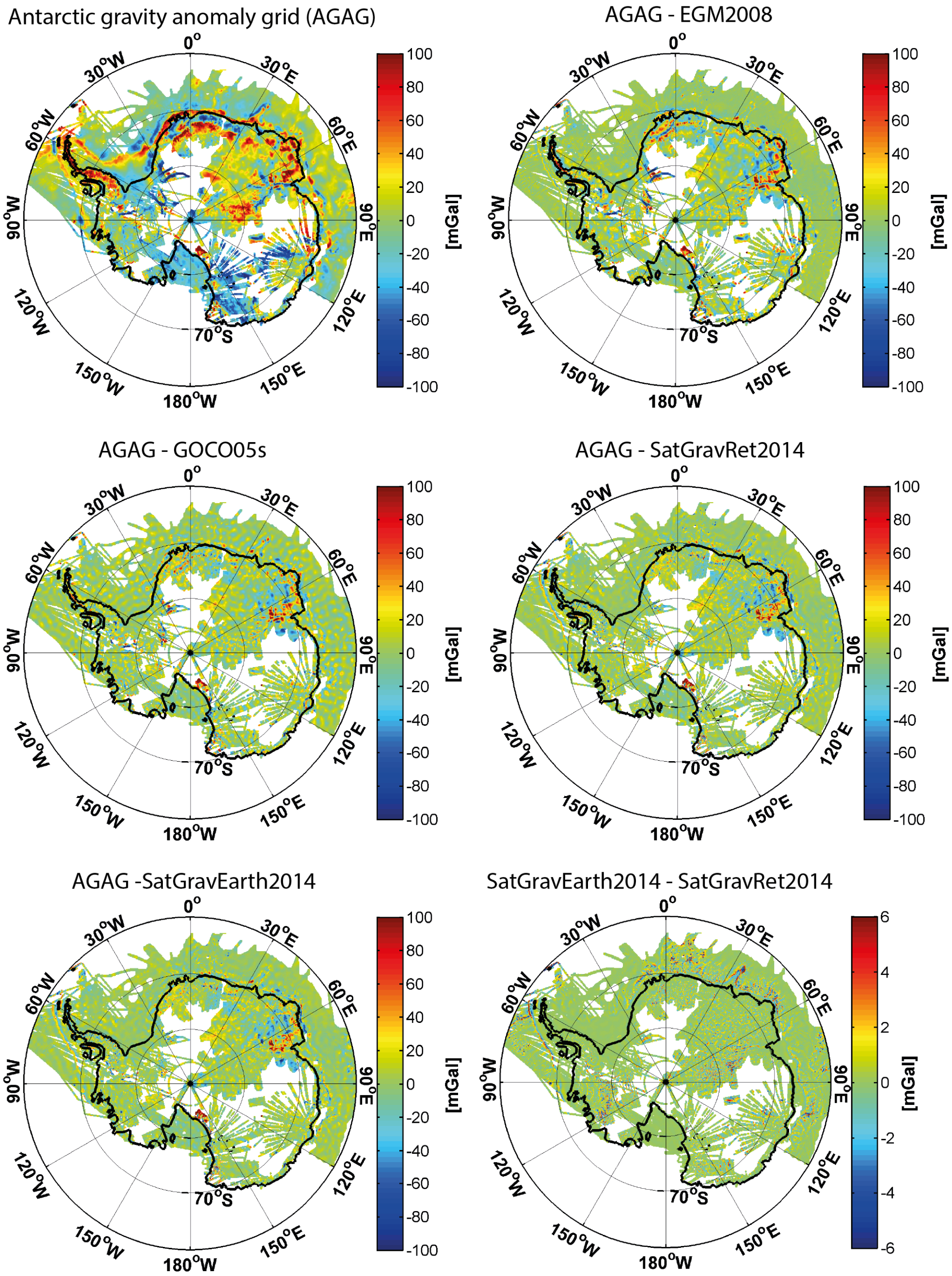

Fig. 12 Antarctic gravity anomaly grid (upper left plot) and residuals with gravity anomalies synthesised from various GGMs (unit is in mGal).

(1% improvement). Globally, this tendency was shown already in Fig. 9. Note that EGM2008 shows a better performance over the ocean than the other investigated models. This is to be expected and reflects that AGAG data and EGM2008 are observation based down to short scales. EGM2008 has DTU altimetry data included over the oceans while AGAG over the oceans presumably relies on ship-track-based observations; hence, both data sets are observation-based and thus in closer agreement than the AGAG observations with forward models. Also, this finding reveals limitations in currently available Antarctic bathymetry data.

The sum of 1) GOCO05s taken (from $n = 0$) up to degree 280 and 2) ETP model (dV_ELL_RET2014 or

Symb.	Term	Direction	Meaning	Use in this work
N	geoid height	normal to ellipsoid	diff. between h and H	none
$\tilde{H}$	mean-sea-level height	appr. normal to geoid	distance: MSL to P_s	given by DEMs and used for H
H	orthometric height	normal to geoid	distance: geoid to P_s	used to approximate the heights in STP and ETP modelling
h	ellipsoidal height	normal to ellipsoid	distance: ellipsoid to P_s	unusable in the modelling because of direction
d	mapped ellipsoidal height	direction to geocenter	distance: ellipsoid to P_m	in ETP modelling under ellipsoidal approximation
h'	pseudo-ellipsoidal height	direction to geocenter	distance: ellipsoid to P_s	can be used in ETP modelling to avoid mapping
D^{sph}	mapped spherical height	direction to geocenter	distance: sphere to P_m	in STP modelling under spherical approximation
H^{sph}	spherical height	direction to geocenter	distance: sphere to P_s	in STP modelling (theoretically)

Table 9 Definition of heights and their usage in this work (see also Fig. 13); P_s: surface point; P_m: mapped surface point; MSL: mean sea level.

dV_ELL_Earth2014) taken in the band $281 \leq n \leq 2190$ shows less agreement with AGAG data (~ 1 mGal more in terms of RMS/STD, see Tab. 8) than the combination models that also comprise gravity from GRACE, GOCE and ETP model (SatGravRET2014 and SatGravEarth2014). Thus, a quite simple combination of the ETP and observed gravity, e.g. as done here by means of a regularisation, is better than omission error modelling, since the latter leads to higher residuals. Omission error modelling means the estimation of short-scale gravity signals that are not contained in a GGM (i.e. signals beyond the maximum degree N of the model) by band limited information that can, e.g., be computed from a residual terrain model (RTM modelling, c.f. Forsberg (1984)) or taken from a (abrupt) truncation of a topographic potential model, as done here.

4.5 Modelling differences between the spherical and ellipsoidal approach

The spherically approximated (see Sect. 2.1) and ellipsoidally approximated (see Sect. 2.2) layer-based forward-modelling of the potential in spherical harmonics – leading to solutions of the STP and ETP, respectively – are to be treated and interpreted differently. The STP and ETP are inherently different regarding the spectral and spatial-domain characteristics as will be shown next.

4.5.1 Geometric differences and mapping of the layer boundaries

Essentially, both STP and ETP are different representations of the (same) potential that is generated by the same masses which are defined by volumetric layers (see Sect. 2 and 3). The spherical approach assumes the boundaries of the layers to be referenced to some reference sphere. This is accomplished with the orthometric height serving as an approximation for the distance between sphere and surface point (referred to as mapped spherical height). The ellipsoidal approach assumes the layers to be referenced to some reference ellipsoid using the orthometric height as approximation for the distance between ellipsoid and surface point (referred to as mapped ellipsoidal height). See also Table 9 for an overview of the used heights, their definitions and

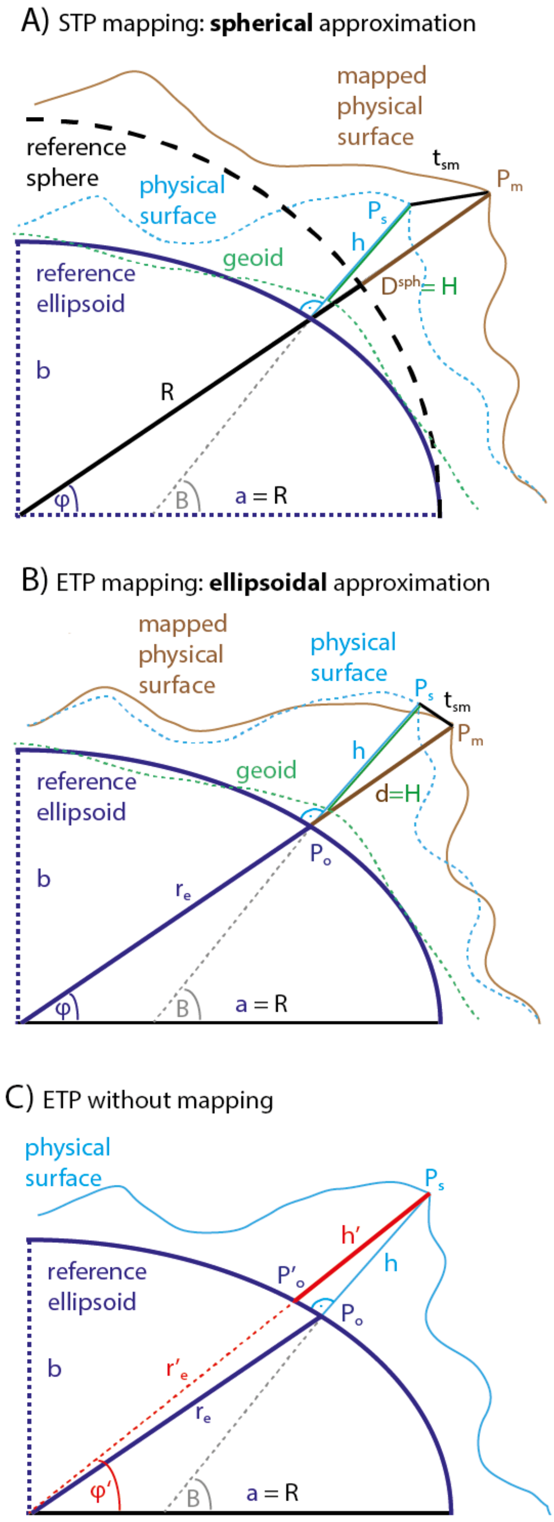

Fig. 13 Scheme of mapping of the Earth's physical surface in the investigated modelling techniques: mapping situation in STP-modelling in spherical approximation (panel A), mapping situation in ETP-modelling in ellipsoidal approximation (panel B) and mapping-free situation in ETP-modelling without approximation by using pseudo-ellipsoidal heights h' at their respective latitudes φ' (panel C); φ:geocentric latitude; B:geodetic latitude; r_e: ellipsoidal radius to P_o; r'_e: ellipsoidal radius to P'_o; a, b: semi-major/minor axis of ellipsoid; R: spherical radius; H:orthometric height; h:ellipsoidal height; D^{sph}: mapped spherical height; d:mapped ellipsoidal height; P_s: surface point; P_m: mapped surface point; t_{sm}:distance $\overline{P_s P_m}$.

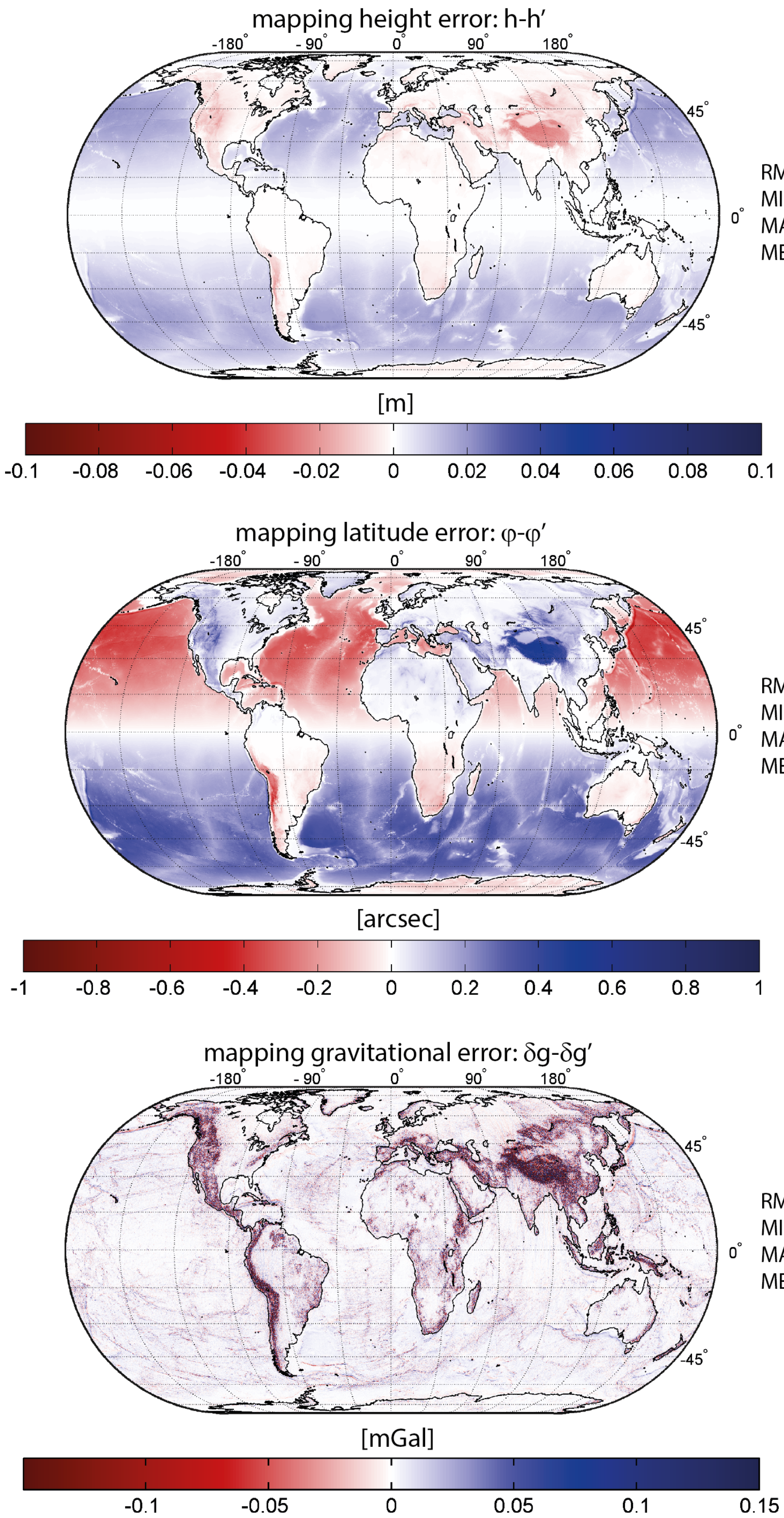

Fig. 14 Mapping effects in the ETP in terms of height differences $h - h'$ (in metres, upper plot), latitude differences $\varphi - \varphi'$(in arc-seconds, middle plot) and the resulting gravity disturbance differences $\delta_g - \delta_g'$ (in mGal, lower plot) of both geometric effects. Note, the effects are also contained in the mapping within the STP, but projected onto the sphere.

use. Neither of the approaches thus takes into account the geoid-ellipsoid separation (i.e. the geoid height), which shall not be further looked at here, nor the fact that orthometric heights are not measured along the direction to the geocenter, which is implicitly assumed in the spherical harmonic framework.

The result of the latter is a displacement (often referred to as mapping) of the Earth's physical surface and of all layer boundaries (Fig. 13). In case of the spherical approximation (STP) the approximation error introduced by the mapping is hard to be determined/interpreted, since the masses and computation point P_S are rearranged w.r.t. a spherical reference (Fig. 13, panel A) and there is no workaround to avoid a displacement of masses. In case of the ellipsoidal approximation (ETP), the displacement due to mapping is largest at mid-latitudes and becomes zero at the poles and the equator (Fig. 13 B and Fig. 14). These displacements are also a part of the mapping within the STP, but (additionally) projected onto the sphere. At maximum, consider a point P_s with extreme elevation of $h = 9$ km above or $h = -10$ km below the ellipsoid and at a latitude of $B = 45°$, the displacement given by the distance $t_{sm} = \overline{P_s P_m}$ between surface point P_s and its mapped equivalent P_m becomes ~ 30 m or 33 m, respectively (i.e. $\varphi - \varphi' \sim 0.9''$ and $h - h' \sim 5$ cm). This confirms similar the findings by Balmino et al (2012). In view of 10km-resolution models as computed in this model mass displacements of this order hardly play a role. Nevertheless, in case of the ETP, displacement can be avoided by working with what we denote pseudo-ellipsoidal heights h' (c.f. Appendix A for their computation). They are given at their respective geocentric latitudes φ' that are defined along the direction towards the geocenter (Fig. 13, panel C). Working with the pseudo-ellipsoidal heights instead of mapped ellipsoidal heights within layer-based modelling to degree 2190 yields differences in the order of ± 3 mGal or RMS=0.04 mGal (see Fig. 14). Accounting for the mapping is thus only required for applications of high accuracy or high resolution.

4.5.2 Differences in the spectral domain

The spherical harmonic coefficients of STP and ETP differ notably as can be seen from their degree variances (Fig. 15). The degree variances of the STP (dV_SPH_Earth2014_lca/lra) follow Kaula's rule (Kaula, 1966) closely, which itself is close to the truly ellipsoidal harmonic spectrum of the gravity field (Rexer and Hirt, 2015a). The degree variances of the ETP (dV_ELL_Earth2014_lca/lra) run below those of STP. They are comparable to commonly used gravity field models (e.g. those listed at ICGEM). This has already been found by Rexer and Hirt (2015a), who empirically derived an approximate rule of thumb that allows to transform degree variances from a spherically approximated model (STP) into their ellipsoidally approximated equivalents (ETP) (and vice versa). All spherical harmonic GGMs (of N $>$ 2000) that (implicitly) assume an ellipsoidal Earth are accompanied by a “tail“of 30 degrees (from degree 2160 to 2190) with rapidly decreasing energy, which are needed for a proper representation of the potential. This is the very reason why band limited investigation are not possible with this kind of models (see Sect. 4.3) without suffering

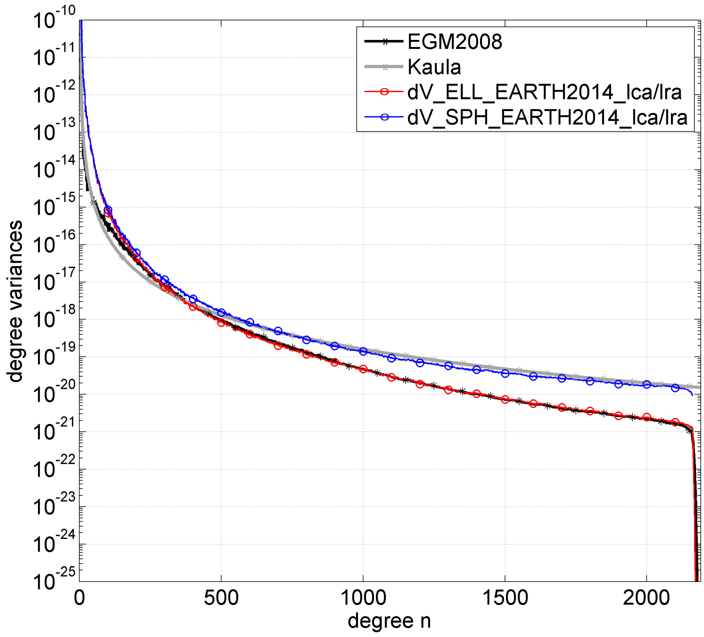

Fig. 15 Spectral characteristics of the spherically (dV_SPH_Earth2014_lca/lra) and the ellipsoidally (dV_ELL_Earth2014_lca/lra) approximated potential models in terms of degree variances, together with those of EGM2008 and Kaula's rule of thumb.

from erroneous striations increasing with latitude (see also Claessens and Hirt (2013); Pavlis et al (2012)). Spherical harmonic models in spherical approximation allow band limited investigations akin to truly ellipsoidal harmonic models (see Sect. 4.3).

4.5.3 Differences in the space domain

In the space domain rather long wavelength differences appear between the STP and the ETP at the level of few mGals (Fig. 16). Note that for a comparison of ETP and STP in the space domain, the ETP was evaluated on the surface of the reference ellipsoid while the STP was evaluated on the surface of the reference sphere. Similar differences were already found to reflect different mass arrangements between ETP and STP by Claessens and Hirt (2013) (ibid. Fig. 6a) who applied the HC-method to a single-density mass model. At the Earth's surface the effect is almost of the same dimension with marginally smaller amplitudes and similar RMS (Fig. 17). The differences in Figs. 16 and 17 also contain the effect of mapping discussed above (h vs. h' and φ vs. φ'), but they are dominated by the additional mapping of the masses from the ellipsoid onto the sphere.

The differences notably differ from the *ellipsoidal correction* (Fig. 12 in Balmino et al (2012)) which is thought to correct a STP model for the difference between integrating Earth's masses w.r.t. spherical instead of an ellipsoidal reference. The range of the *ellipsoidal correction* in Balmino et al (2012) is much smaller (~ 0.005 mGal vs. ~ 8 mGal) – even when investigating the differences in Fig. 16 in the same spectral band ($0 \leq n \leq 120$) – and is predominated by a zonal J_2 effect. Possibly, their correction, which is only computed

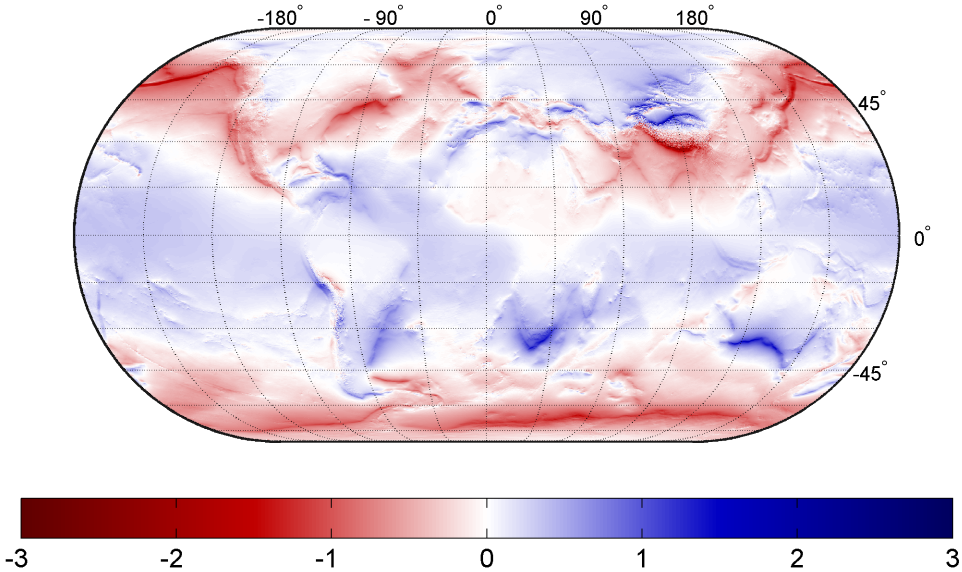

Fig. 16 Gravity difference between the spherically (dV_SPH_Earth2014_lca/lra) and the ellipsoidally (dV_ELL_Earth2014_lca/lra) approximated potential models in terms of gravity disturbances evaluated **at the respective reference surface (sphere and ellipsoid, respectively)**; $RMS = 0.35$ mGal;$min = -4.66$ mGal ;$max = 2.84$ mGal; $mean = -0.08$ mGal. (unit is in mGal)

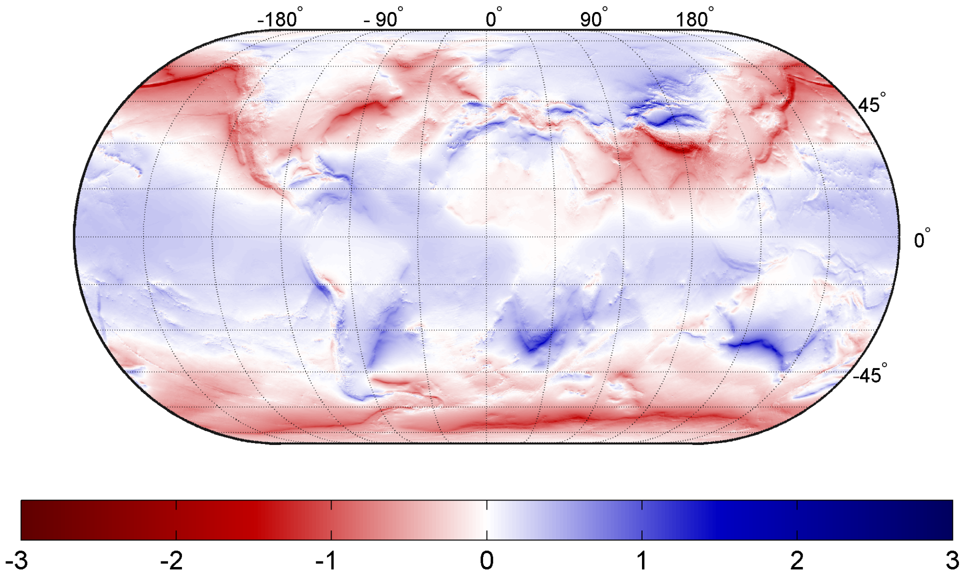

Fig. 17 Gravity difference between the spherically (dV_SPH_Earth2014_lca/lra) and the ellipsoidally (dV_ELL_Earth2014_lca/lra) approximated potential models in terms of gravity disturbances evaluated **at the Earth's surface**; $RMS = 0.36$ mGal;$min = -2.89$ mGal ;$max = 2.11$ mGal; $mean = -0.08$ mGal. (unit is in mGal)

to the second order, is a part of the true difference between a topographic forward model in spherical and ellipsoidal approximation.

5 Conclusions and outlook

We presented spectral forward modelling based on volumetric mass layers to d/o 2190 at two different levels of approximation (spherical and ellipsoidal) and took full account of increased sampling requirements and all relevant terms of the involved binominal series expansions, avoiding aliasing and truncation errors due to early truncation of the series.

Based on the HCM-method, we derived a new spherical harmonic approach that allows to rigorously and efficiently compute the ellipsoidally approximated topographic potential based on volumetric layers of laterally varying density that are referenced to an ellipsoid. A layer-concept has been established with the layers' boundaries taken from the Earth2014 model, separating the masses of ice-sheets, water in inland lakes/seas, ocean water and solid rock with $1'$ resolution. Applying the layer-concept in two ways – in a correction approach with actual densities or in a reduction approach with density contrasts – leads to equivalent potentials, with negligible differences (RMS~ 0.001 mGal) that are caused by the spherical harmonic representation of the respective layer boundaries. The layer-based modelling approach reaches over 90 % correlation with EGM2008 in the band $900 \leq n \leq 2150$ with significantly higher correlations compared to single-density (RET) modelling. Further, it was shown to be at least equivalent to state-of-the-art layer-based forward modelling in the space domain. A validation with ground truth gravity data over Antarctica shows that layer-based modelling improves over single-density modelling by $\sim 2\%$, with the improvement being largest over the ocean ($\sim 5\%$). The latter was also confirmed globally by computing reduction rates with GOCE satellite observations as contained in GO_CONS_GCF_2_TIM_R5. For the validation we computed a combination model, combining computed spherical harmonic coefficients in ellipsoidal approximation with satellite observations from GOCE and GRACE satellite, which is necessary in order to mitigate the problem of isostatically uncompensated masses in the forward models. The combination was done by means of an empirical regularisation of GOCE and GRACE normal equations. Using solely the most accurate ground truth observations ($STD < 2$ mGal) available, the combination model was found superior to EGM2008 and the satellite-only model GOCO05s (by $\sim 25\%$ and $\sim 8\%$ in terms of RMS). The comparison with ground truth data also showed that a combination of satellite data with the topographic potential, e.g. by means of a regularization, is to be preferred compared to omission error modelling in general.

Depending on the level of approximation – spherical or ellipsoidal – we provided the framework to the spherical topographic potential (STP) or the ellipsoidal topographic potential (ETP), which were found to have substantially different spectral characteristics, yet rather small differences in the space domain. Evaluated at the respective reference surface or at surface of Earth the STP and ETP show differences at the level of $\sim \pm 5$ mGal ($RMS = 0.4$ mGal) that mainly stem from a different arrangement of masses (mapping) due to different geometric assumptions in the approaches. In ellipsoidal approximation the mapping, which was found to cause a rearrangement of masses by 30 m at maximum, can completely be avoided by using pseudo-ellipsoidal heights that are measured towards the geocenter. The error introduced by the mapping is in the order of mGal and should be taken into account in applications requiring ultra-high resolution or high accuracy topographic gravity.

In the spectral domain, the STP shows substantially larger energy at short scales (comparable to that predicted by Kaula's rule of thumb or to the truly ellipsoidal harmonic spectrum of EGM2008) than the ETP. The ETP shows short scale energy comparable to other spherical harmonic GGMs that make an (implicit) ellipsoidal assumption of Earth, e.g. EGM2008. This feature makes the ETP coefficients suitable for a combination with satellite data, e.g. as done in this work. The dependencies among the spherical harmonic coefficients in ellipsoidal approximation prevent application of the harmonic models in a band-limited manner (i.e. no truncations at $n < 2190$). In contrast, spherical harmonic models in spherical approximation and truly ellipsoidal harmonic models are free of such dependencies and may be used in band limited form (i.e. truncated at $n < 2190$).

In conclusion, the choice between spherical and ellipsoidal approximation in spectral forward modelling depends on the application of the final models. While STP models may be good enough for a wide range of geophysical applications, ETP models are more accurate and needed for high resolution applications. Current observation based gravitational models conform spectrally with the ellipsoidal topographic potential which is inevitable for geodetic applications, such as a combination with satellite and terrestrial data by means of regularization.

The herein computed models are available at: *http://ddfe.curtin.edu.au/models/Earth2014/potential_model/*.

A Rigorous expressions - direct solution to the radial integral in modelling of the ETP and the STP

In contrast to the above presented solutions to the STP (Sec. 2.1) and ETP (Sec. 2.2) that rely on a binominal series expansion for the solution of the radial integral (Eq. 17), and in case of the ETP also on the binominal series expansion in Eq. 27, here the rigorous expressions are given.

The direct (rigorous) solution to the radial integral over the masses in a layer (Eq. 10) was given already in Eq. 11 or (in more generalised form) in Eq 13, respectively.

A.1 Rigorous solution to the STP of a volumetric mass layer

In case of the STP, the direct integral solution to the radial integral from the lower to the upper layer bound in spherical approximation reads

$$\Omega^{(STP,\omega)} = \rho^{(\Omega_\omega)}(\theta_Q,\lambda_Q)\frac{R}{n+3}\left(\left(\frac{R+H_{UB}^{(\Omega_\omega)}}{R}\right)^{n+3} - \left(\frac{R+H_{LB}^{(\Omega_\omega)}}{R}\right)^{n+3}\right). \tag{37}$$

Inserting Eq. 37 into Eq. 9 the rigorous expression of the STP of a volumetric mass layer is

$$\hat{V}_{nm}^{(STP,\Omega_\omega)} = \frac{3}{\overline{\rho}(2n+1)(n+3)} \times$$
$$\times\frac{1}{4\pi}\int_{\lambda=0}^{2\pi}\int_{\theta=0}^{\pi}\rho^{(\Omega_\omega)}(\theta_Q,\lambda_Q)\left(\left(\frac{R+H_{UB}^{(\Omega_\omega)}}{R}\right)^{n+3} - \left(\frac{R+H_{LB}^{(\Omega_\omega)}}{R}\right)^{n+3}\right)\overline{Y}_{nm}(\theta_Q,\lambda_Q)\sin\theta d\theta d\lambda, \tag{38}$$

and with

$$\overline{HDF}_{nnm}^{(STP,\Omega\omega)} = \frac{1}{4\pi}\int_{\lambda=0}^{2\pi}\int_{\theta=0}^{\pi}\rho^{(\Omega_\omega)}(\theta_Q,\lambda_Q)\left(\left(\frac{R+H_{UB}^{(\Omega_\omega)}}{R}\right)^{n+3} - \left(\frac{R+H_{LB}^{(\Omega_\omega)}}{R}\right)^{n+3}\right)\overline{Y}_{nm}(\theta_Q,\lambda_Q)\sin\theta d\theta d\lambda. \tag{39}$$

we arrive at the more concise form

$$\hat{V}_{nm}^{(STP,\Omega_\omega)} = \frac{3}{\overline{\rho}(2n+1)(n+3)}\,\overline{HDF}_{nnm}^{(STP,\Omega\omega)}. \tag{40}$$

As mentioned above rigorous expressions for the STP of a layer in principal are known already in different notation, e.g. by Pavlis and Rapp (1990). The disadvantage of the rigorous expression in Eq. 40 is that it needs n_{max} spherical harmonic analyses of the surface function $\overline{HDF}_{nnm}^{(STP,\Omega\omega)}$, while the expression relying on a binominal series expansion (Eq. 21) only needs k_{max} analyses, where $k_{max} << n_{max}$ in general (see Sec. 2.3 for convergency behavior of the binominal series).

A.2 Rigorous solution to the ETP of a volumetric mass layer

In case of the ETP, the direct integral solution to the radial integral from the lower to the upper layer bound in ellipsoidal approximation reads

$$\Omega^{(ETP,\omega)} = \rho^{(\Omega_\omega)}(\theta_Q,\lambda_Q)\frac{R}{n+3}\left(\frac{r_e}{R}\right)^{n+3}\left(\left(\frac{r_e+d_{UB}^{(\Omega_\omega)}}{r_e}\right)^{n+3} - \left(\frac{r_e+d_{LB}^{(\Omega_\omega)}}{r_e}\right)^{n+3}\right). \tag{41}$$

Inserting Eq. 41 into Eq. 9 the rigorous expression of the ETP of a volumetric mass layer is

$$\hat{V}_{nm}^{(ETP,\Omega_\omega)} = \frac{3}{\overline{\rho}(2n+1)(n+3)} \times$$
$$\times\frac{1}{4\pi}\int_{\lambda=0}^{2\pi}\int_{\theta=0}^{\pi}\rho^{(\Omega_\omega)}(\theta_Q,\lambda_Q)\left(\frac{r_e}{R}\right)^{n+3}\left(\left(\frac{r_e+d_{UB}^{(\Omega_\omega)}}{r_e}\right)^{n+3} - \left(\frac{r_e+d_{LB}^{(\Omega_\omega)}}{r_e}\right)^{n+3}\right)\overline{Y}_{nm}(\theta_Q,\lambda_Q)\sin\theta d\theta d\lambda, \tag{42}$$

and with

$$\overline{HDF}_{nnm}^{(ETP,\Omega\omega)} = \frac{1}{4\pi}\int_{\lambda=0}^{2\pi}\int_{\theta=0}^{\pi}\rho^{(\Omega_\omega)}(\theta_Q,\lambda_Q)\left(\frac{r_e}{R}\right)^{n+3}\times$$
$$\times\left(\left(\frac{r_e+d_{UB}^{(\Omega_\omega)}}{r_e}\right)^{n+3} - \left(\frac{r_e+d_{LB}^{(\Omega_\omega)}}{r_e}\right)^{n+3}\right)\overline{Y}_{nm}(\theta_Q,\lambda_Q)\sin\theta d\theta d\lambda. \tag{43}$$

we arrive at the more concise form

$$\hat{V}_{nm}^{(ETP,\Omega_\omega)} = \frac{3}{\overline{\rho}(2n+1)(n+3)}\ \overline{HDF}_{nnm}^{(ETP,\Omega\omega)}. \tag{44}$$

The disadvantage of the rigorous expression in Eq. 44 is that it needs n_{max} spherical harmonic analyses of the surface function $\overline{HDF}_{nnm}^{(ETP,\Omega\omega)}$, while the expression relying on binominal series expansions (Eq. 31) only needs k_{max} analyses, where $k_{max} << n_{max}$ in general (see Sec. 2.3 for convergency behavior of the binominal series).

B Computation of the pseudo-ellipsoidal height h' and its latitude φ' of the surface point P_S

Given a surface point P_S with ellipsoidal height h, geodetic latitude B and geocentric distance r defined by

$$r^2 = (r'_e + h')^2 \tag{45}$$

the pseudo-ellipsoidal height h' that is running along the direction towards the geocenter (Fig. 18) can be computed using the cosine rules

$$r^2 = c^2 + ((N - e^2N) + h)^2 - 2c((N - e^2N) + h)\cdot\cos(\pi - B) \tag{46}$$

where

$$c = e^2 N\cos B, \tag{47}$$

$$N = \frac{a}{\sqrt{1 - e^2\cdot\sin^2 B}} \tag{48}$$

and

$$r_e'^2 = a^2\frac{1-e^2}{1-e^2\cdot\cos^2\varphi'}. \tag{49}$$

The (geocentric) latitude φ' can be computed using the sine rule

$$\sin\varphi' = \left(\frac{((N-e^2N)+h)\cdot\sin(\pi - B)}{r}\right). \tag{50}$$

Then the pseudo-ellipsoidal height is retrieved with

$$h' = r - r'_e. \tag{51}$$

Acknowledgements This study received support from the German National Research Foundation (DFG), project n° Hi 1760/1. It was also supported by the Technische Universität München - Institute for Advanced Study, funded by the German Excellence Initiative (and the European Union Seventh Framework Programme under grant agreement n° 291763). We also acknowledge the Czech Ministry of Education, Youth and Sport for a financial support by the

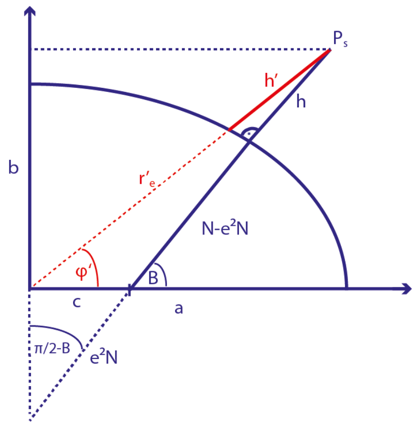

Fig. 18 Ellipsoidal height h and pseudo ellipsoidal height h'.

National Program of Sustainability, Project No.: LO1506. We thank Simon Holmes and NGA for the distribution of the land/ocean masks used in the creation of EGM2008. We further thank Simon Holmes for generously sharing the software facilitating Jekeli's transform with us. We thank Torsten Mayer-Gürr and Jan-Martin Brockmann for providing the satellite gravity normal equations for this study. We further acknowledge the work of all other producers of data used in this work. Finally, we thank two anonymous reviewers for their detailed reviews.

References

Amante C, Eakins B (2009) ETOPO1 1 Arc-Minute Global Relief Model: Procedures, Data Sources and Analysis. NOAA Technical Memorandum NESDIS NGDC-24, National Geophysical Data Center, NOAA

Balmino G, Lambeck K, Kaula W (1973) A spherical harmonic analysis of the earth's topography. Journal of Geophysical Research 78(2):478–521

Balmino G, Vales N, Bonvalot S, Briais A (2012) Spherical harmonic modelling to ultra-high degree of bouguer and isostatic anomalies. Journal of Geodesy 86(7):499–520, DOI 10.1007/s00190-011-0533-4, URL http://dx.doi.org/10.1007/s00190-011-0533-4

Bartusch M, Berg H, Siebertz O (2008) The TanDEM-X Mission. In: Synthetic Aperture Radar (EUSAR), 2008 7th European Conference on, pp 1–4

Brockmann J, Zehentner N, Höck E, Pail R, Loth I, Mayer-Gürr T, Schuh W (2014) EGM_TIM_RL05: An Independent Geoid with Centimeter Accuracy Purely Based on the GOCE Mission. Geophysical Research Letters 41(22):8089–8099, DOI 10.1002/2014GL061904

Bucha B, Janák J (2014) A MATLAB-based graphical user interface program for computing functionals of the geopotential up to ultra-high degrees and orders: Efficient computation at irregular surfaces. Computers and Geosciences 66:219–227

Chen W, Tenzer R (2014) Harmonic coefficients of the Earth's Spectral Crustal Model 180 – ESCM180. Earth Science Informatics 8(1):147–159, DOI 10.1007/s12145-014-0155-5, URL http://dx.doi.org/10.1007/s12145-014-0155-5

Claessens S (2006) Solutions to Ellipsoidal Boundary Value Problems for Gravity Field Modelling. PhD thesis, Curtin University of Technology

Claessens S, Hirt C (2013) Ellipsoidal topographic potential - new solutions for spectral forward gravity modelling of topography with respect to a reference ellipsoid. Journal of Geophysical Research 118(11):5991–6002, DOI 10.1002/2013JB010457

Fecher T, Pail R, Gruber T (2013) Global gravity field modeling based on GOCE and complementary gravity data. International Journal of Applied Earth Observation and Geoinformation 35:120–127, DOI 10.1016/j.jag.2013.10.005

Forsberg R (1984) A study of terrain reductions, density anomalies and geophysical inversion methods in gravity field modelling. OSU Report 355, Ohio State University

Forsberg R, Jensen T (2015) New geoid of Greenland: A case study of terrain and ice effects, GOCE and the use of local sea level data. International Association of Geodesy Symposia DOI 10.1007/1345_2015_50

Göttl F, Rummel R (2009) A Geodetic View on Isostatic Models. Pure and Applied Geophysics 166:1247–1260, DOI 10.1007/s00024-004-0489-x

Grombein T, Seitz K, Heck B (2013) Optimized formulas for the gravitational field of a tesseroid. Journal of Geodesy 87:645–660, DOI 10.1007/s00190-013-0636-1

Grombein T, Luo X, Seitz K, Heck B (2014) A Wavelet-Based Assessment of Topographic-Isostatic Reductions for GOCE Gravity Gradients. Surveys in Geophysics pp 1–24, DOI 10.1007/s10712-014-9283-1, URL http://dx.doi.org/10.1007/s10712-014-9283-1

Grombein T, Seitz K, Heck B (2016) The Rock-Water-Ice Topographic Gravity Field Model RWI_TOPO_2015 and Its Comparison to a Conventional Rock-Equivalent-Version. Surveys in Geophysics 37(5):937–976, DOI 10.1007/s10712-016-9376-0

Heck B, Seitz K (2007) A comparison of the tesseroid, prism and point-mass approaches for mass reductions in gravity field modelling. Journal of Geodesy 81:121–136, DOI 10.1007/s00190-006-0094-0

Heiskanen W, Moritz H (1967) Physical Geodesy. WH Freeman Comp

Hirt C (2012) Efficient and accurate high-degree spherical harmonic synthesis of gravity field functionals at the Earth's surface using the gradient approach. Journal of Geodesy 86(9):729–744

Hirt C, Kuhn M (2014) A band-limited topographic mass distribution generates a full-spectrum gravity field - gravity forward modelling in the spectral and spatial domain revisited. Journal of Geophysical Research - Solid Earth 119(4):3646–3661, DOI doi:10.1002/2013JB010900

Hirt C, Rexer M (2015) Earth2014: 1' shape, topography, bedrock and ice-sheet models - Available as gridded data and degree 10,800 spherical harmonics. International Journal of Applied Earth Observation and Geoinformation DOI 10.1016/j.jag.2015.03.001

Hirt C, Gruber T, Featherstone W (2011) Evaluation of the first GOCE static gravity field models using terrestrial gravity, vertical deflections and EGM2008 quasigeoid heights. Journal of Geodesy 85:723–740

Hirt C, Kuhn M, Featherstone W, Göttl F (2012) Topographic/isostatic evaluation of new-generation GOCE gravity field models. Journal of Geophysical Research - Solid Earth 117:B05,407, DOI 10.1029/2011JB008878

Hirt C, Claessens S, Fecher T, Kuhn M, Pail R, Rexer M (2013) New ultra-high resolution picture of Earth's gravity field. In: Hirt et al (2013), DOI 10.1002/grl.50838

Hirt C, Rexer M, Scheinert M, Pail R, Claessens S, Holmes S (2015) A new degree-2190 (10 km resolution) gravity field model for Antarctica developed from GRACE, GOCE and Bedmap2 data. Journal of Geodesy 90:105–127, DOI 10.1007/s00190-015-0857-6

Jekeli C (1988) The exact transformation between ellipsoidal and spherical harmonic expansions. manuscripta geodaetica 13(2):106–113

Kaula W (1966) Theory of Satellite Geodesy. Blaisdel, Waltham

Kuhn M, Hirt C (2016) Topographic gravitational potential up to second-order derivatives: an examination of approximation errors caused by rock-equivalent topography (ret). Journal of Geodesy (online first) 90(9):883–902, DOI 10.1007/s00190-016-0917-6

Kuhn M, Seitz K (2005) Comparison of newton's integral in the space and frequency domains. In: Sanso F (ed) A window on the Future of Geodesy - IAG Symposia, vol 128, pp 386–391

Laske G, Masters G, Ma Z, Pasyanos M (2012) CRUST1. 0: An updated global model of Earth's crust. Geophys Res Abs 14

Lee W, Kaula W (1967) A spherical harmonic analysis of the Earth's Topography. Journal of Geophysical Research 72:753–758

Mayer-Gürr T, Kurtenbach E, Eicker A (2010) ITG-Grace2010 Gravity Field Model. , www.igg.uni-bonn.de/apmg/index.php?id=itg-grace2010

Mayer-Gürr T, Pail R, Gruber T, Fecher T, Rexer M, Schuh WD, Kusche J, Brockmann JM, Rieser D, Zehentner N, Kvas A, Klinger B, Baur O, Höck E, Krauss S, Jäggi A (2015) The combined satellite gravity field model goco05s. In: Presentation at EGU 2015, Vienna, April2015

Nagy D, Papp G, Benedek J (2000) The gravitational potential and its derivatives for the prism. Journal of Geodesy 74:552–560, DOI 10.1007/s00190-006-0094-0

Nagy D, Papp G, Benedek J (2002) Correction to "the gravitational potential and its derivatives for the prism". Journal of Geodesy 76:475, DOI 10.1007/s00190-002-0264-7

Pail R, Fecher T, Jäggi A, Goiginger H (2011) Can GOCE help to improve temporal gravity field estimates? In: Ouwehand L (ed) Proceedings of the 4th International GOCE User Workshop, ESA Publication SP-696

Pasyanos M, Masters T, Laske G, Ma Z (2014) LITHO1.0 : An updated crust and lithospheric model of the Earth. Journal of Geophysical Research: Solid Earth 119(3):2153–2173

Pavlis N, Factor J, Holmes S (2007) Terrain-related gravimetric quantities computed for the next egm. In: Dergisi H (ed) Proceedings of the 1st International Symposium of the International Gravity Field Service, vol 18, pp 318–323

Pavlis N, Holmes S, Kenyon S, Factor J (2012) The developement and evaluation of the Earth Gravitational Model 2008 (EGM2008). Journal of Geophysical Research 117, DOI 10.1029/2011JB008916

Pavlis NK, Rapp R (1990) The development of an isostatic gravitational model to degree 360 and its use in global gravity modelling. Geophys J Int 100:369–378

Rapp R (1982) Degree Variances of the Earth's Ptential, Topography and its Isostatic Compensation. Bulletin Géodéesique 65:84–94

Rexer M, Hirt C (2015a) Spectral analysis of the Earth's topographic potential via 2D-DFT: a new data-based degree variance model to degree 90,000. Journal of Geodesy 89(9):887–909, DOI 10.1007/s00190-015-0822-4

Rexer M, Hirt C (2015b) Ultra-high-Degree Surface Spherical Harmonic Analysis Using the Gauss-Legendre and the Driscoll/Healy Quadrature Theorem and Application to Planetary Topography Models of Earth, Mars and Moon. Surveys in Geophysics 36(6):803–830, DOI 0.1007/s10712-015-9345-z

Rexer M, Hirt C (2016) Evaluation of intermediate TanDEM-X digital elevation data products over Tasmania using other digital elevation models and accurate heights from the Australian National Gravity Database. Australian Journal of Earth Sciences (accepted for publication)

Rexer M, Hirt C, Claessens S, Braitenberg C (2015) Use of topography in the context of the GOCE satellite mission - some examples. In: Ouwehand L (ed) Proc. '5th International GOCE User Workshop', Paris, France, 25-28 November 2014, ESA Communications, ESA SP-728

Root B, Novák P, Dirkx M, Kaban M, van der Wal W, Vermeersen L (2016) On a spectral method for forward gravity field modelling. Journal of Geodynamics 97:22–30, URL http://dx.doi.org/10.1016/j.jog.2016.02.008

Rummel R, Rapp R, Sünkel H, Tscherning C (1988) Comparisons of Global Topographic/Isostatic Models To the Earth's Observed Gravity Field. OSU report 388, Ohio State University

Saleh J, Pavlis N (2002) The Development and Evaluation of the Global Digital Terrain Model DTM2002. In: 3rd Meeting of the International Gravity and Geoid Commission, Thessaloniki, Greece

Sanso F, Sideris M (2013) Geoid Determination - Lecture Notes in Earth Sciences, vol 110, Springer-Verlag Berlin Heidelberg, chap Harmonic Calculus and Global Gravity Models

Scheinert M, Ferraccioli F, Schwabe J, Bell R, Studinger M, Damaske D, Jokat W, Aleshkova N, Jordan T, Leitchenkov G, Blankenship DD, Damiani TM, Young D, Cochran JR, Richter TD (2016) New antarctic gravity anomaly grid for enhanced geodetic and geophysical studies in antarctica. Geophysical Research Letters 43(2):600–610, DOI 10.1002/2015GL067439, URL http://dx.doi.org/10.1002/2015GL067439, 2015GL067439

Sun W, Sjöberg L (2001) Convergence and optimal truncation of binominal expansions used in isostatic compensations and terrain corrections. Journal of Geodesy 74:627–636

Tenzer R, Abdalla A, Vajda P, Hamayun (2010) The spherical harmonic representation of the gravitational field quantities generated by the ice density contrast. Contrib Geophys Geod 40(3):207–223

Tenzer R, Chen W, Tsoulis D, Bagherbandi M, Sjöberg L, Novák P, Jin S (2015) Analysis of the refined CRUST1. 0 crustal model and its gravity field. Surveys in Geophysics 36(1):139–165

Tenzer R, Hirt C, Novák P, Pitoňák M, Šprlák M (2016) Contribution of mass density heterogeneities to the quasigeoid-to-geoid separation. Journal of Geodesy 90(1):65–80, DOI 10.1007/s00190-015-0858-5

Wieczorek M (2007) Treatise on Geophysics, vol 10, Elsevier, chap The gravity and topography of the terrestrial planets, pp 165–206. DOI 10.1016/B978-044452748-6/00156-5

Wieczorek M (2015) Treatise on Geophysics - 2nd Edition, vol 10, Elsevier, chap The gravity and topography of the terrestrial planets, pp 153–193